A&A 594, A47 (2016)
DOI: 10.1051/0004-6361/201629004

Astronomy & Astrophysics

# First theoretical global line lists of ethylene ($^{12}C_2H_4$) spectra for the temperature range 50−700 K in the far-infrared for quantification of absorption and emission in planetary atmospheres⋆

M. Rey[1], T. Delahaye[2], A. V. Nikitin[3,4], and Vl. G. Tyuterev[1]

[1] Groupe de Spectrométrie Moléculaire et Atmosphérique, UMR CNRS 7331, BP 1039, 51687 Reims Cedex 2, France
e-mail: `michael.rey@univ-reims.fr`
[2] Laboratoire Interuniversitaire des Systèmes Atmosphériques (LISA, CNRS UMR 7583), Université Paris Est Créteil, Université Paris Diderot, Institut Pierre-Simon Laplace, 94010 Créteil, France
[3] Laboratory of Theoretical Spectroscopy, Institute of Atmospheric Optics, SB RAS, 634055 Tomsk, Russia
[4] Laboratory of Quantum Mechanics of Molecules and Radiative Processes, Tomsk State University, 36 Lenin Avenue, 634050 Tomsk, Russia

Received 26 May 2016 / Accepted 8 July 2016

## ABSTRACT

We present the construction of complete and comprehensive ethylene line lists for the temperatures 50−700 K based on accurate ab initio potential and dipole moment surfaces and extensive first-principle calculations. Three lists spanning the [0−6400] $cm^{-1}$ infrared region were built at $T = 80$, 160, and 296 K, and two lists in the range [0−5200] $cm^{-1}$ were built at 500 and 700 K. For each of these five temperatures, we considered possible convergence problems to ensure reliable opacity calculations. Our final list at 700 K was computed up to $J = 71$ and contains almost 60 million lines for intensities $I > 5 \times 10^{-27}$ cm/molecule. Comparisons with experimental spectra carried out in this study showed that for the most active infrared bands, the accuracy of band centers in our theoretical lists is better on average than 0.3 $cm^{-1}$, and the integrated absorbance errors in the intervals relevant for spectral analyses are about 1−3%. These lists can be applied to simulations of absorption and emission spectra, radiative and non-LTE processes, and opacity calculations for planetary and astrophysical applications.

**Key words.** methods: laboratory: molecular – molecular data – radiative transfer

## 1. Introduction

Molecular species in the atmospheres of various astrophysical objects such as giant planets are primarily hydrogen and hydrocarbons. Of all hydrocarbons, ethylene ($^{12}C_2H_4$), which is the simplest alkene, is highly important in various domains of science. In the Earth's atmosphere, it is known as a pollutant produced by forest fires (Rinsland et al. 2009; Goode et al. 1999), volcanic emissions, and also by road traffic and plants (Abeles et al. 1992) that affect the ozone concentration. Together with other simple hydrocarbons such as methane, acetylene, or ethane (see, e.g., Nixon et al. 2007; Sada et al. 1998, 2005; Maltagliati et al. 2015 and references therein), ethylene is very interesting for various planetological and astrophysical applications. These hydrocarbons dominate the opacity of some brown dwarfs and asymptotic giant branch (AGB) stars and are considered to be standard building blocks for carbon-rich atmospheres of many exoplanets (Hu & Seager 2014). The upper atmosphere of an exoplanet can be efficiently probed by transit techniques and transmission spectroscopy (Swain et al. 2010), which are excellent diagnostic tools for understanding physical chemistry under elevated temperature conditions (Tinetti et al. 2013).

Ethylene was detected in Jupiter's atmosphere, where methane is photolyzed by solar radiation to yield $C_2$ hydrocarbons. Measurements of individual emission spectral lines on Jupiter were reported in Kostiuk et al. (1989) and further used to determine the molecular abundances. More recently, emission ethylene spectra have been measured in the poles and equator of Jupiter by Romani et al. (2008), making this molecule the ideal candidate for studying the auroral process in the stratosphere. It has been also detected on Jupiter and Saturn in non-auroral regions (Bézard et al. 2001). The analysis of the mass and distributions of $C_2H_4$ on the Jupiter-orbiting comet SL9 was presented in Griffith et al. (1997), and the investigation of the photochemistry on some hydrocarbons from the Infrared Space Observatory (ISO) observations was reported by Moses et al. (2000). Again in Saturn, ethylene has recently been detected in the hot temperature beacon (Hesman et al. 2012) region using the Composite Infrared Spectrometer (CIRS) with strong thermal emission at 10.5 μm. Various studies of ethylene and other hydrocarbons on Neptune, mini-Neptunes, and Titan were also reported (Schulz et al. 1999; Hu & Seager 2014; Vinatier et al. 2010; Coustenis et al. 1991, 1989, 2007; Coustenis & Bézard 1995; Vinatier et al. 2007; Yang et al. 2012; Canosa et al. 2007; Roe et al. 2004; Wang et al. 2009). In particular, $C_2H_4$ is the only molecular species on Titan whose mixing ratio decreases with height at latitudes below 46°N (Vinatier et al. 2010). It also

---

⋆ The lists are freely accessible through the TheoReTS information system at `http://theorets.univ-reims.fr` and `http://theorets.tsu.ru` plays a role in the formation mechanism of benzene in Titan's atmosphere through the reaction with $C_4H_2^+$ to form the precursor $C_6H_5^+$ (Yang et al. 2012). Additionally, photoabsorption, photodissociation, and photoelectron spectroscopic studies of ethylene have been reported (see Cooper et al. 1995; Holland et al. 1997; Wu et al. 2004) with measurements of the temperature-dependent cross-section in the VUV region between 118 and 192 nm.

Accurate knowledge of line intensities in the infrared and their temperature dependence is essential for reliable remote sensing. In particular, the 3.3 and 1.6 $\mu$m regions are generally dominated by strong absorption bands of hydrocarbons such as methane, ethane, and ethylene, which correspond to the fundamental and first overtones in C-H stretching modes. However, the analysis of the rotationally resolved ethylene spectra is complex above 2000 cm$^{-1}$ because of resonance interactions and very dense rotational patterns that are due to the twelve vibrational modes. Despite a considerable number of studies (see Sect. 2 for a non-exhaustive list of references), laboratory data analyses in several spectral intervals are incomplete. Most of them only concern line positions, whereas intensity measurements and calculations remain quite sparse. A significant number of hot-band transitions contribute to the ethylene opacity even at room temperature because the torsion modes lie below 1000 cm$^{-1}$. Because of difficulties in analyses of congested laboratory infrared spectra, the ethylene line-by-line information in available spectroscopic databases (Rothman et al. 2013; Jacquinet-Husson et al. 2011), essentially composed of cold-band transitions from the ground state, is far from being complete for accurate opacity calculations. No high-temperature laboratory intensity data are available.

This work aims at providing first exhaustive theoretical line lists of ethylene for planetology and astrophysical application in the range 50 K–700 K in the far-infrared covering all fundamental and overtone combinations and hot bands up to 5200 cm$^{-1}$. The paper is structured as follows. Section 2 briefly overviews available line-by-line laboratory analyses. The methods for accurate first-principle global spectra calculations and ab initio based line lists of this work are described in Sect. 3. Section 4 is devoted to comparing our results with empirical HITRAN room-$T$ database (Rothman et al. 2013) and PNNL experimental spectral records (Johnson et al. 2004). We also discuss the completeness problems in available lists. Our calculations agree very well with experiments for ranges in which data exist, but represent a very significant extension in terms of the number of transitions and the spectral coverage. Temperature effects on spectra are discussed in Sect. 5. An additional extension up to 6400 cm$^{-1}$ is considered in Sect. 6, and in Sect. 7 we discuss opacity convergence and spectral quasi-continuum problems at various temperatures.

## 2. Current state of analyses of ethylene experimental laboratory spectra

The analysis and modeling of the infrared ethylene spectra is much less advanced than for four- and five-atomic hydrocarbon molecules, $C_2H_2$ and $CH_4$, that have higher symmetry. As a consequence of the $D_{2h}$ symmetry of $C_2H_4$, the ro-vibrational levels do not show strict degeneracies; the twelve vibrational modes of ethylene make the infrared spectrum very dense and complex, with typical asymmetric top molecules $J$, $K_\mathrm{a}$, $K_\mathrm{c}$ structures. The fundamental vibrational modes cover a quite wide spectral range, from torsion (~800 cm$^{-1}$) to stretching (~3000 cm$^{-1}$) bands, with no simple relations between corresponding frequencies. In contrast to the methane molecule, ethylene vibrations do not show a clear polyad structure, except for the relatively narrow 10 $\mu$m region (see, e.g., Fig. 1, which is explained the next section). Dense vibrational sequences composed of fundamentals, overtones, and combination bands cause many accidental resonances, which results in vast perturbations in ro-vibrational spectra and in intensity-borrowing effects among strong and weaker transitions.

The most extensive empirical model for the ethylene vibrational levels to date has been considered by Georges et al. (1999) based on the information from previous high-resolution studies (Lambeau et al. 1982; Sartakov et al. 1997; Rusinek et al. 1998; Bach et al. 1999; Oomens et al. 1996, 1994a,b). In the entire data set, spectral analyses remain quite sparse: of the 200 vibrational bands up to 4000 cm$^{-1}$, only 16 were completely or partially modeled. Many line-by-line analyses have focused on the 10 $\mu$m region using spectroscopic empirical models (Blass et al. 2001; Rotger et al. 2008; Vander Auwera et al. 2014; Tan et al. 2000; Ulenikov et al. 2013); Alkadrou et al. (2016), either for each band individually or simultaneously for the so-called tetrad $\nu_{10}/\nu_4/\nu_7/\nu_{12}$. Analyses of high-resolution Fourier transform spectra in the 4.3–5.6 $\mu$m region were reported by Lafferty et al. (2011), Ben Hassen et al. (2012). This included the six vibrational bands $\nu_7+\nu_8/\nu_4+\nu_6/\nu_6+\nu_{10}/\nu_6+\nu_7/\nu_4+\nu_6/\nu_3+\nu_{10}$. A quite crude model in the ($\nu_9/\nu_{11}$) dyad approximation was employed to analyze high-resolution spectra in the 3 $\mu$m region (Lorono et al. 2010). Corresponding effective spectroscopic parameters and the rovibrational eigenfunctions had to compensate for contributions of many other missing bands. An accurate and proper modeling of line intensities that are affected by the model truncations proved to be a very difficult task. To describe line positions in this region, a larger set of 32 vibrational combination states coupled with $\nu_9/\nu_{11}$ through cubic anharmonicity and Coriolis interaction was considered in Sartakov et al. (1997). This led to an empirical determination of additional centers. In addition, molecular jet double-resonance spectroscopy in the 3 $\mu$m region permitted a preliminary study of line positions in $\nu_7+\nu_9-\nu_7$, $\nu_7+\nu_{11}-\nu_7$ and $\nu_{10}+\nu_{11}-\nu_{10}$ hot-band systems (Oomens et al. 1994a,b; Dam et al. 1990). A high-resolution study of the $\nu_5+\nu_{12}$ band near 2.2 $\mu$m was reported in Ulenikov et al. (2010). A preliminary analysis of line positions the 1.6 $\mu$m region was carried out using a very crude effective model, including only the $\nu_5+\nu_9/\nu_5+\nu_{11}$ system (Lorono et al. 2010). A series of papers was devoted to the study of ethylene isotopologs (see De Vleeschouwer et al. 1982; Flaud et al. 2011, 2010; Tan et al. 2015b,a; Ulenikov et al. 2015; Gabona et al. 2014; Gabona & Tan 2014a,b; Tan & Gabona 2012, and references therein). Most available analyses of ethylene laboratory spectra only consider line positions. Integrated band intensities from low-resolution spectra have been measured by Lebron & Tan (2012). Few works in the literature were devoted to absolute intensity measurements in rotationally resolved spectra (Blass et al. 2001; Rotger et al. 2008; Vander Auwera et al. 2014; Lafferty et al. 2011; Ben Hassen et al. 2012); Alkadrou et al. (2016) but ethylene line-by-line intensity data above 3 $\mu$m range are essentially missing.

## 3. Theory and computational methods

The aim of this work is to fill the gaps in ethylene laboratory data by constructing comprehensive theoretical line lists in the far-infrared from molecular potential energy surface (PES) and dipole moment surfaces (DMS) that are sufficiently complete

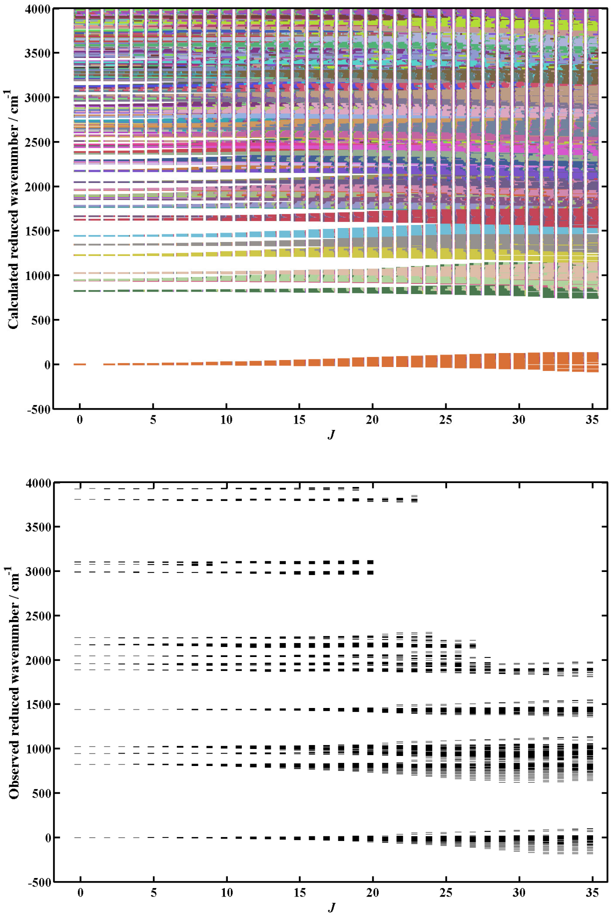

**Fig. 1.** Reduced energy levels $E_{vJ} - E^{r.r.}$ for ethylene for the 155 000 variationally predicted vibration-rotation levels (*upper panel*) and for the 10 600 observed levels (*lower panel*). $E^{r.r.}$ are the rigid rotor energy levels taken as $0.9J(J+1) + 4.05K_a^2$.

for astrophysical applications in the considered temperature conditions.

Ab initio studies of small polyatomic molecules emerged in the past decades with drastically improved computational methods and hardware resources. A breakthrough in predicting rotationally resolved spectra of small molecules was made possible by accurate electronic structure calculations of the molecular PESs and DMSs (see, e.g., Partridge & Schwenke 1997; Cours et al. 2002; Yurchenko et al. 2009; Nikitin et al. 2009; Lodi et al. 2011; Császár et al. 2010; Szalay et al. 2011; Huang et al. 2011a, 2012; Sousa-Silva et al. 2014; Nikitin et al. 2014; Li et al. 2014; Delahaye et al. 2015) and by developing efficient methods for quantum nuclear motion calculations (see Schwenke & Partridge 2001; Schwenke 2002; Cassam-Chenaï et al. 2012; Yurchenko et al. 2007; Wang & Carrington Jr. 2013a,b; Carter et al. 2009; Rey et al. 2012; Bowman et al. 2005). In case of triatomics, such as water isotopic species (Yurchenko et al. 2009; Barber et al. 2011), carbon dioxide (Huang et al. 2013, 2014), and ozone (Tyuterev et al. 2013b, 2014) accurate theoretical predictions led to significant extensions of spectral analyses toward higher energy ranges. Theoretical line lists for ammonia (Huang et al. 2011a,b; Yurchenko et al. 2009) and phosphine (Yurchenko et al. 2006; Sousa-Silva et al. 2014; Nikitin et al. 2014; Rey et al., in prep.) are successful examples of such a trend for four-atomics. Accurate first principles of rovibrational spectra of five-atomic molecules such as methane and its isotopologs have been reported in Rey et al. (2013a,b, 2014a,b, 2015a,b). Recently, high-temperature theoretical line lists for astrophysical applications have been constructed for methane in Warmbier et al. (2009), Tennyson et al. (2013), Yurchenko & Tennyson (2014), Rey et al. (2014b).

The first fourth-order ab initio force-field calculations of ethylene were performed by Martin et al. (1995). A series of theoretical studies based on a modified Martin PES were reported by Avila & Carrington Jr. (2011) and by Carter et al. (2012b,a), who also published qualitatively correct ab initio intensity predictions for fundamental and lower combination bands. In our previous works, we reported further improvement of ab initio calculations that resulted in more accurate PES (Delahaye et al. 2014) and DMS (Delahaye et al. 2015). Global calculations of rotationally resolved spectra involving hot bands for six-atomic systems such as ethylene remain a challenging problem mainly because convergence issues as the CPU and memory requirements increase very rapidly with the number of atoms. To our knowledge, no full-dimensional line lists of ethylene have been published before this work.

### *3.1. Global variational calculations of ethylene vibration-rotation level and transition intensities*

To construct ethylene line-by-line lists accounting for all transitions that might contribute to the absorption or emission at a given temperature, we used full quantum-mechanical calculations. The infrared intensities $S_{if}$ of ro-vibrational transitions $\nu_{if}$ for a given temperature $T$ are defined as

$$S_{if} = \frac{8\pi^3 10^{-36}}{3hcQ(T)} g_{C_i} \nu_{if} \mathrm{e}^{-c_2 E_i/T}(1 - \mathrm{e}^{-c_2 \nu_{if}/T})\mathcal{R}_{if} \tag{1}$$

in standard spectroscopic units cm$^{-1}$/(molecule cm$^{-2}$) ≡ (further denoted for simplicity as cm/molecule), where $c_2 = hc/k$ with $k$ the Boltzmann constant, $g_{C_i}$ and $E_i$ are the nuclear spin statistical weight and the energy of the lower state. $Q(T)$ is the partition function.

The line strength of a dipole-allowed rovibrational transition $f \leftarrow i$ is defined as

$$\mathcal{R}_{if} = \sum_{MM'} |\, \langle i \,|\, \mu \,|\, f \rangle \,|^2, \tag{2}$$

where the summation is over all magnetic sublevels of both initial and final states. The dipole moment components $(\mu_X, \mu_Y, \mu_Z)$ of $\mu$ are given in the laboratory-fixed frame (LFF) and $|\, i\rangle$, $|\, f\rangle$ are eigenfunctions of the Hamiltonian. Owing to the isotropy of space (in the absence of an electric field), each space-fixed component contributes equally to the line strength. Accordingly, we write $\mathcal{R}_{if} = 3\mathcal{R}^Z_{if}$. The ab initio dipole moment is computed in the molecular-fixed frame (MFF), whose components $\mu_\beta$ $(\beta = x, y, z)$ are related to those of the LFF under the rotation $R$ defining the direction cosines $\lambda_{\alpha\beta}$, as $\mu_Z = \sum_\beta \lambda_{Z\beta}\mu_\beta$. Finally, we can write

$$\mathcal{R}_{if} = 3 \sum_{MM'} |\, \langle (\Psi^{(J',C')}_{M',\sigma'})_i \,|\, \sum_\beta \lambda_{Z\beta}\mu_\beta(R_1, R_2, \cdots, R_N) \,|\, (\Psi^{(J,C)}_{M,\sigma})_f \rangle \,|^2 \,. \tag{3}$$

In short notations, $|\, \Psi_i\rangle \equiv|\, i\rangle$, $|\, \Psi_f\rangle \equiv|\, f\rangle$ are the Hamiltonian eigenfunctions for the initial and final ro-vibrational states, characterized by the total angular momentum $(J', J)$ and symmetry blocks $(C', C)$. Thus computation of $\mathcal{R}_{if}$ consists of evaluating the vibrational matrix elements $\langle v'_1, v'_2, \cdots \,|\, \mu_\beta \,|\, v_1, v_2, \cdots \rangle$ and of

**Table 1.** Fundamental vibrational band centers of $^{12}C_2H_4$ from the initial and refined (this work, TW) DNRST PES.

| Band | Initial PES (Delahaye et al. 2014) | Refined PES (TW) | Obs. (Georges et al. 1999) |
|---|---|---|---|
| $\nu_1(A_g)$ | 3018.99 | 3021.91 | 3021.85 |
| $\nu_2(A_g)$ | 1624.43 | 1626.43 | 1626.17 |
| $\nu_3(A_g)$ | 1342.46 | 1343.28 | 1343.31 |
| $\nu_4(A_u)$ | 1024.94 | 1025.61 | 1025.58 |
| $\nu_5(B_{2g})$ | 3079.86 | 3082.51 | 3082.36 |
| $\nu_6(B_{2g})$ | 1224.26 | 1225.46 | 1225.41 |
| $\nu_7(B_{2u})$ | 949.51 | 948.78 | 948.77 |
| $\nu_8(B_{3g})$ | 934.29 | 939.83 | 939.86 |
| $\nu_9(B_{3u})$ | 3101.69 | 3105.00 | 3104.87 |
| $\nu_{10}(B_{3u})$ | 822.42 | 825.84 | 825.92 |
| $\nu_{11}(B_{1u})$ | 2985.38 | 2988.37 | 2988.63 |
| $\nu_{12}(B_{1u})$ | 1441.11 | 1442.54 | 1442.44 |

**Notes.** All values are given in $\mathrm{cm}^{-1}$.

the rotational factors $\langle J', K', M' |\ \lambda_{Z\beta}\ | J, K, M\rangle$. The first are computed in a quite straightforward manner, while for the second, it is computationally advantageous to consider spherical tensors (Bunker & Jensen 1998).

The temperature $T$ is involved as a macroscopic parameter affecting the population of the vibrational and rotational states through the Boltzmann factor. A modeling of absorption or emission spectra at a given temperature will require at least four quantities: the line positions ($\nu_{if}$), the line intensities ($S_{if}$), the lower state energies ($E_i$), and the partition function ($Q(T)$). To this end, three main theoretical ingredients are necessary:

(i) A full 12D intra-molecular PES in a wide range of vibrational displacements to compute the wavefunctions $\Psi$'s and to predict ro-vibrational energy levels $E_i$ and line positions $\nu_{if}$. The accuracy of the quantities $E_i$, $v$, $Q$ and $\Psi$ in Eq. (1) depends explicitly on the quality of the PES. In this work, we used our previous ab inito potential (hereafter referred to as DNRST PES, Delahaye et al. 2014) as a starting surface. To further improve the accuracy of the ab initio PES, we slightly refined the quadratic force constants $F_{ij}$ directly related to the harmonic oscillator frequencies to better match the experimental fundamental band centers. Some details of this procedure and the values of optimized force constants are given in the Appendix. Fundamental band centers obtained with this empirically optimized PES are given in Table 1 with the rms (obs.-calc.) deviation of $\sim$0.3 $\mathrm{cm}^{-1}$.

(ii) DMS components $\mu_\beta$ defined in a wide range of nuclear configurations $\{R_1, R_2, \cdots, R_N\}$ are necessary to calculate transition probabilities between upper and lower vibration-rotation states. The accuracy of line strength calculations will depend on both the PES and DMS through the functions $\Psi$ and the dipole moment components. In this work we employ our recent ab initio DNRST DMS (Delahaye et al. 2015). This DMS has permitted an improvement of the accuracy of line intensity predictions in the fundamental ethylene bands by an order of magnitude with respect to previous ab initio calculations (Carter et al. 2012b,a). The accuracy of the line intensities for the fundamental bands is $\sim$1–6%.

(iii) Efficient computational methods for quantum mechanical motions to achieve a good numerical convergence of calculations in a large basis set with a full account of molecular symmetry properties. In contrast to effective empirical spectroscopic models that deal with finite-dimensional matrices, variational calculations face the well-known problem of the basis set convergence. This problem becomes extremely challenging when the number of atoms is increased, particularly for high values of the total angular momentum $J$ that are necessary for high-temperature predictions.

The ethylene molecule possesses 12 vibrational and 3 rotational degrees of freedom for the nuclear motion. This is by 3 degrees of freedom larger than in a five-atomic system (such as in methane, the largest molecule for which full high-$T$ rotationally resolved spectra predictions have been published to date; Rey et al. 2014b; Yurchenko & Tennyson 2014). To give an idea of the challenge, we can estimate that each additional vibrational degree of freedom would increase the matrix dimensions in brute force computations by roughly one order of magnitude.

In this work, we applied vibrational normal modes and an Eckart frame representation (Watson 1968) for the nuclear motion, a basis set of wavefunctions and dipole moment expansion, the formalism of which is described in Rey et al. (2010, 2012). To minimize the cost of computations and loss of precision in full-dimensional variational calculations, we implemented truncation-compression techniques as described in our previous works for methane isotopologs and ethylene (see Rey et al. 2013a,b, 2014a; Delahaye et al. 2014). The validity and the accuracy studies of our ab initio surfaces and convergence tests for energy levels, eigenfunctions, and intensities have been determined and reported in previous studies (Rey et al. 2015b), also using independent computational methods and program implementations by Nikitin et al. (2012) and Tyuterev et al. (2013a). In this work, the Hamiltonian model is that of Delahaye et al. (2014), while the vibrational and ro-vibrational basis sets were slightly enlarged to allow a better convergence, as outlined in the Appendix.

A global set of vibration-rotation energy levels $E_{vJ}$ was computed here up to rotational quantum numbers $J \leq 71$ to ensure the completeness of our line lists for $T = 700$ K and below. The additional difficulty was that the necessary $J_{\max} = 71$ cutoff is much higher than in all available methane calculations because the ethylene molecule is heavier. In Fig. 1, we plot only a small part ($J < 35$) of our variationally predicted reduced energy levels $E_{vJ} - E^{r.r.}$ and compare them to those assigned from analysis (Blass et al. 2001; Rotger et al. 2008; Vander Auwera et al. 2014; Ulenikov et al. 2013; Lafferty et al. 2011; Ben Hassen et al. 2012); Alkadrou et al. (2016). To match the scale of the figure, all levels were shifted by the values of the rigid rotor energy levels $E^{r.r.}$. The first conclusion is that variational calculations bring $\sim$93% more information than available analyses in the range 0–4000 $\mathrm{cm}^{-1}$. The expected effect of the missing transitions on the opacity calculation in some spectral regions could be significant, especially for modeling hot spectra that involve high $J$ values. The other information in this figure is the complex eigenvector redistribution as $J$ and $E$ increase. Each color in the upper panel represents a mixing coefficient $(c_i^j)^2$ of the wavefunction decomposition $\Psi_j = c_1^j\phi_1 + c_2^j\phi_2 + \cdots$, such that $\sum_k (c_k^j)^2 = 1$. This means that effective spectroscopic polyad models usually employed in empirical analyses show their limits. Polyads of closely lying ro-vibrational states that are clearly separated from other groups are no more clearly defined above 1500 $\mathrm{cm}^{-1}$ and for $J > 20$.

Overlapping vibration-rotation patterns as shown in Fig. 1 generally lead to numerous perturbations in spectra and very many poorly defined parameters in empirical models that are

**Table 2.** Values of the partition function $Q(T)$ calculated from the direct sum and the direct product (see text).

| | | | | Direct product | Direct sum |
|---|---|---|---|---|---|
| $T(K)$ | Refs. | $Q_{\mathrm{vib}}$ | $Q_{\mathrm{rot}}$ | $Q_{\mathrm{vib}}Q_{\mathrm{rot}}$ | $Q_{\mathrm{dir}}$ |
| 80 | TW[a] | 1 | 1471.7 | 1471.7 | 1471.7 |
| | Blass et al. (2001) | 1 | 1467.9 | 1467.9 | |
| | HITRAN | | | 1474.2 | |
| 160 | TW[a] | 1.0011 | 4154.0 | 4158.6 | 4158.8 |
| | Blass et al. (2001) | 1.0009 | 4143.4 | 4147.1 | |
| | HITRAN | | | 4169.4 | |
| 296 | TW[a] | 1.0521 | 10448.4 | 10 992.8 | 10997.8 |
| | Blass et al. (2001) | 1.0469 | 10 421.4 | 10910.1 | |
| | HITRAN | | | 11 041.5 | |
| | $D_{2h}$TDS, Rotger (2016) | | 10 447.7 | | |
| | Carter et al. (2012b) | | | | 10979.2 ($J \leq 40$) |
| | Rotger et al. (2008) | 1.0469 | 10432.9 | 10 922.2 | |
| 500 | TW[a] | 1.4396 | 22951.3 | 33 040.7 | 33117.2 |
| | HITRAN | | | 33271.3 | |
| 700 | TW[a] | 2.4274 | 38048.0 | 92 357.7 | 92702.8 |
| | HITRAN | | | 93 244.0 | |

**Notes.** [(a)] TW = this work.

commonly applied for laboratory spectrum analyses. A determination of resonance coupling parameters from experimental levels is known to be a mathematically ill-defined problem (see Perevalov et al. 1984, 1985). Extrapolation capabilities of effective spectroscopic models critically depend on the range of available data included in the fit, limited information for inactive bands, dark state perturbations, and various ambiguity problems. This could result in an unreliable description of resonance intensity transfers between strong and weaker bands. For example, the 3 $\mu$m region has been recently modeled with only two interacting vibrational bands, namely $\nu_{11}/\nu_9$, while 25 vibrational bands fall in the region 2900−3200 cm$^{-1}$. As a direct consequence, Hamiltonian parameters of the $\nu_{11}/\nu_9$ dyad may not allow a proper modeling of the observed data, and some dipole moment parameters are generally overestimated to compensate for the missing band contributions. For this reason, an extrapolation of the synthetic spectrum obtained from cold or room temperature empirical data analyses to different temperature conditions could fail.

### 3.2. Temperature dependence of the partition function

Temperature-dependent modeling of gaseous atmospheres also requires knowledge of the molecular partition function (PF) $Q(T)$ involved in Eq. (1). The total internal partition function (PF) of a molecule can be expressed as a direct sum of Boltzmann factors at a given temperature:

$$Q_{\mathrm{dir}}(T) = \sum (2J+1) g_{\mathrm{C}} \exp(-c_2 E_{vJ}/T). \tag{4}$$

This requires calculating all energy levels $E_{vJ}$ up to a maximum value $E_{\mathrm{max}}$ for which $Q(T)$ converges. Because of the large number of terms in the direct sum, spectroscopic effective models for polyatomic modules are not appropriate for the PF evaluation in a consistent manner as many computed energy levels are missing (see Fig. 1, lower panel, for example). A useful approximation is often used in the literature that consists of evaluating the PF by the direct product $Q_{\mathrm{prod}}(T) \approx Q_{\mathrm{vib}}Q_{\mathrm{rot}}$, by ignoring vibration-rotation interactions. We list in Table 2 the PF from the direct sum and from the direct product approximation and compare it to the values available in the literature. For this work, $Q_{\mathrm{vib}}$ was calculated from the variational energies obtained with the $F(11)$ basis and $Q_{\mathrm{rot}}$ from the rotational energies for $J \leq 71$ obtained with the ro-vibrational basis sets $F(5)$ and $F(6)$ (see Appendix).

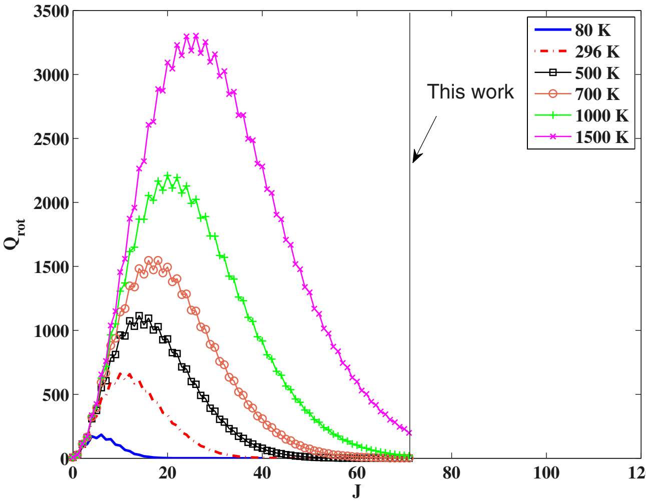

**Fig. 2.** Convergence of the rotational partition function $Q_{\mathrm{rot}}$ as a function of the total angular momentum $J$ for ethylene.

Figure 2 displays our variationally predicted rotational PF as a function of $J$. We see that with $J_{\mathrm{max}} = 71$ the $Q_{\mathrm{rot}}$ fully converges for the temperatures considered in this work (orange circles in Fig. 2 for $T \leq 700$ K). Extensive calculations, both in vibration and rotation, are necessary to consider higher temperatures. A rough estimate suggests that the values $J_{\mathrm{max}} \approx 80$–85

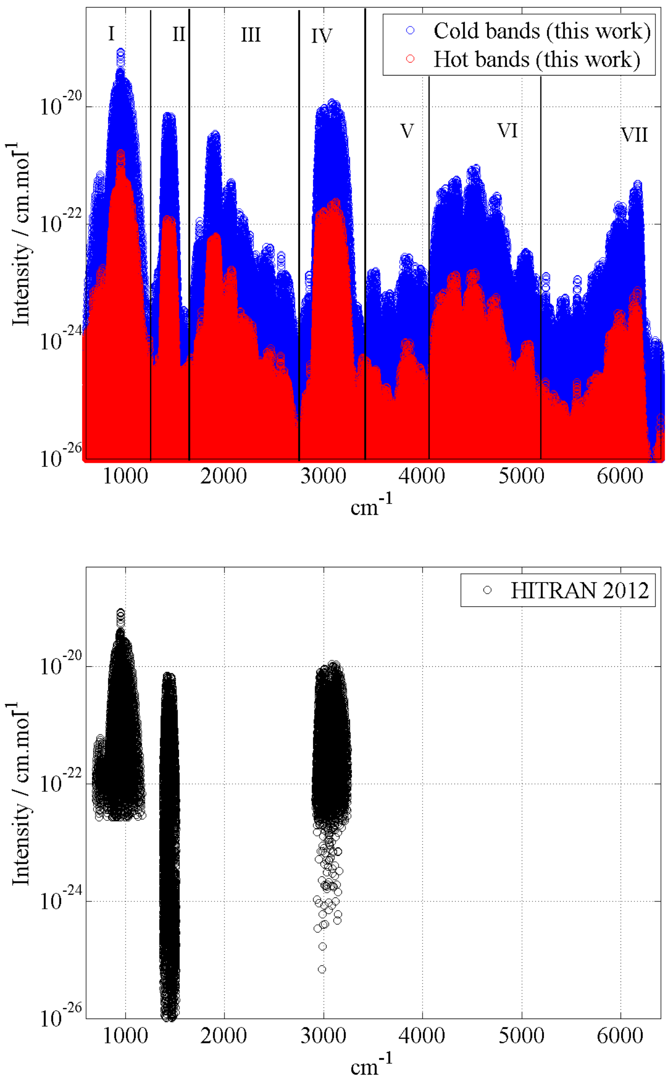

**Fig. 3.** Overview spectrum of ethylene from 0 to 6400 cm$^{-1}$: comparison between theoretical predictions using molecular PES and DMS (this work, *top panel*) and the HITRAN 2012 empirical database (*bottom panel*) in log scale. Intensities are in HITRAN units and given at $T$ = 296 K. Contributions of cold- and hot-band transitions are also specified.

and ≈120–130 will be required to compute hot spectrum predictions at 1000 K and 1500 K, respectively.

Our $Q_{\mathrm{rot}}$(296 K) calculation agrees very well with the recent work obtained with the $D_{2h}$TDS software (Rotger 2016). Carter et al. (2012b) reported a value of $Q$(296 K) = 10 979.2 computed up to $J$ = 40 using variational calculations, our direct method gives a very similar result, $Q_{\mathrm{dir}}$ ($J \le 40$) = 10 989.5. We also note that the HITRAN values are slightly overestimated compared to ours, for instance, by about ~0.4% at 296 K. This could be explained by an overestimation of $Q_{\mathrm{vib}}$, which was treated in HITRAN as an infinite sum of harmonic oscillators including artificial bound-state vibrational levels above the dissociation limit.

## 4. Ethylene line lists: completeness problem for empirical databases

At a given temperature $T$, the number of transitions included in our variationally computed theoretical lists is essentially governed by three cutoff parameters: the lowest line intensity ($I_{\mathrm{min}}$), the highest energy of the low-state levels ($E_{\mathrm{low}}$), and the highest value of the rotational quantum number $J$. Each line list cutoff was chosen in a way that the global opacity of ethylene in the considered spectral range converges. The corresponding statistics are discussed in the last section of the paper. Ethylene spectral data in the far-infrared are included in several empirical databases such as HITRAN, GEISA, and EcaSDa (Rothman et al. 2013; Jacquinet-Husson et al. 2011; Ba et al. 2013), and some lines are accessible at the internet portal of the VAMDC center (Rixon et al. 2011; Dubernet-Tuckey et al. 2016). Most of them are based on line-by-line analyses of experimental laboratory room-$T$ spectra. To validate all our results, the calculations were first compared to the last edition of the empirical HITRAN2012 database at $T$ = 296 K. Figure 3 gives the log scale overview comparison in the range up to 6400 cm$^{-1}$ between our room-$T$ line list and HITRAN2012. Clearly, the set of data available in HITRAN, which is essentially composed of nine vibrational bands with 18 000 transitions, is incomplete compared to that provided by our variational calculations, which contain more than 2.9 million transitions at 296 K (with the intensity cutoff $I_{\mathrm{min}} = 10^{-26}$). As already stated above, as a result of its twelve vibrational modes and the absence of clear polyad structures in very congested spectrum, ethylene is a typical example of a molecule absorbing ubiquitously in the infrared. This comparison clearly confirms that an ethylene line-by-line analyses of spectra through polyad effective models have intrinsic limits, in particular for the modeling of line intensities. The experimental measurement, identification, and extraction of individual line intensities for many thousands or even millions of overlapping transitions in the room-$T$ spectrum is clearly not feasible. The low-lying vibrational torsional modes cause a significant number of hot-band transitions ($v_i - v_j$ where $v_j$ are some excited vibrational states) appear even at room temperature with non-negligible intensities. Information on HBs associated with transitions from or to ro-vibrational patterns of highly excited vibrational states is almost lacking or very insufficient in available databases. According to Fig. 3, HBs contribute approximately to 5% of the total opacity at $T$ = 296 K.

Another possible validation of a theoretical list is a comparison of simulated cross-sections (XS) with medium-resolution experimental Fourier-transform laboratory spectra available in the PNNL library (Johnson et al. 2004), which are recorded at temperatures of 5, 25, and 50 °C with a pressure of 1 atm. To simulate spectra at a resolution of 0.01 cm$^{-1}$, a Voigt profile and a self-broadening coefficient of 0.1 cm$^{-1}$ atm$^{-1}$ at 296 K were chosen. In contrast to HITRAN, the PNNL spectra are not assigned. They therefore do not contain line-by-line or low-energy information and cannot be extrapolated beyond their experimental conditions. The comparisons with PNNL spectra are given below in the form of absorbance simulations that are converted into cross sections (in cm$^2$/molecule) using the factor $9.28697 \times 10^{-16}$ [1].

### 4.1. Region (I): 600–1200 cm$^{-1}$

A more detailed comparison of our theoretical list with the empirical HITRAN database and with PNNL spectra at room-$T$ in the spectral range 600–1200 cm$^{-1}$, dominated by the strongest $\nu_7$ band is given in Fig. 4. $\nu_4$ and $\nu_{10}$ also fall in the region that was the subject of several papers. Considering the opacity contribution, the ratio between $\nu_7$, $\nu_{10}$ and $\nu_4$ is approximately

---

[1] See `https://secure2.pnl.gov/nsd/nsd.nsf/Welcome`

**Table 3.** Comparison of the integrated intensities and integrated absorbance of our variational calculation (this work) with the empirical HITRAN and the experimental PNNL databases.

| | Integrated intensities (in cm/molecule) | | | | Integrated absorbance | |
|---|---|---|---|---|---|---|
| Region (cm$^{-1}$) | CB | HB | CB+HB | HT2012 | This work | PNNL |
| (*I*) 600−1200 | 1.35E-17 | 8.43E-19 | 1.44E-17 | 1.29E-17 | 2.54E-1 | 2.62E-1 |
| Nb of lines | 38 753 | 32 6118 | 36 4871 | 5816 | | |
| (*II*) 1200−1600 | 1.61E-18 | 8.99E-20 | 1.70E-18 | 1.59E-18 | 3.01E-2 | 3.07E-2 |
| Nb of lines | 12 215 | 80 675 | 92 890 | 5400 | | |
| (*III*) 1600−2750 | 9.68E-19 | 7.03E-20 | 1.04E-18 | / | 1.833E-2 | 1.89E-2 |
| Nb of lines | 96 027 | 22 8905 | 32 4932 | / | | |
| (*IV*) 2750−3450 | 6.64E-18 | 3.53E-19 | 6.99E-18 | 5.78E-18 | 1.24E-1 | 1.23E-1 |
| Nb of lines | 10 8458 | 40 4403 | 51 2861 | 6881 | | |
| (*V*) 3450−4050 | 3.39E-20 | 1.49E-21 | 3.53E-20 | / | /[a] | |
| Nb of lines | 99 769 | 44 763 | 14 4532 | / | | |
| (*VI*) 4050−5200 | 1.01E-18 | 4.87E-20 | 1.06E-18 | / | 1.87E-2 | 1.86E-2 |
| Nb of lines | 40 6188 | 41 6116 | 82 2304 | / | | |
| (*I*−*VI*)600−5200 | 2.38E-17 | 1.41E-18 | 2.52E-17 | 2.02E-17 | 4.45E-1 | 4.53E-1 |
| Nb of lines | 76 1410 | 15 00980 | 22 62390 | 18 097 | | |

**Notes.** Contribution of the cold (CB) and hot (HB) bands is also listed. (a) See Sect. 4.5 for explanation.

given by 68:2:1. Our list matches the observed ethylene spectra from PNNL very well, where the simulation was made at a resolution of 0.01 cm$^{-1}$ and a pressure of 1 atm. The same is true for the comparison with HITRAN: our predictions agree very well. The upper panel of Fig. 4 shows that some transitions are clearly lacking in HITRAN. Moreover, our global calculations systematically include all hot bands, while they were considered neither in HITRAN (only 140 transitions are tabulated) nor in all recent analyses. Table 3 summarizes the integrated intensities and integrated absorbances for our calculations, HITRAN and PNNL. The hot-band contributions are not negligible. For instance, the $2\nu_7-\nu_7$ and $\nu_7+\nu_{10}-\nu_{10}$ hot bands produce a comparable contribution to the opacity at 296 K as the fundamental $\nu_{10}$ and $\nu_4$ bands. When only cold-band transitions are considered, the calculated integrated intensities deviate by about 5.5% from HITRAN. This slight discrepancy may be partly explained by the fact that our variational calculations include high-$J$ transitions up to $J = 50$ that are lacking in the HITRAN database, which contains six times fewer lines. Even when we apply the same intensity cutoff as in HITRAN2012, that is, $I_{\max} = 10^{-23}$ cm/molecule, we have a larger sample of 11105 transitions in the range 700–1170 cm$^{-1}$ with the integrated range intensity of $1.35 \times 10^{-17}$ cm/molecule that are to be compared to 5816 HITRAN transitions, giving an integrated intensity of $1.28 \times 10^{-17}$ cm/molecule. Note that the HITRAN intensities were divided by the natural abundance factor 0.97729 to rescale it to 100% of abundance. Concerning the comparison with PNNL, our integrated absorbance is underestimated by about 3%. We have to note that PNNL spectra were recorded with natural ethylene. To compensate for ~2% of lacking $^{13}C^{12}CH_4$ lines in our calculations, the ethylene $^{12}C_2H_4$ concentration was set to 100%. Thus we have implicitly assumed that 2% of $^{12}C_2H_4$ provides approximately the same amount of opacity as 2% of $^{13}C^{12}CH_4$. At the resolution used in PNNL spectra, it is quite difficult to distinguish minor isotopologs.

### 4.2. Region (II): 1200–1600 cm$^{-1}$

This region is essentially composed of transitions of the $\nu_{12}$ band and to a lesser extent by $\nu_{12}+\nu_j-\nu_j$ HB transitions with ~4–5% contribution to the total opacity. Again, the agreement of our calculation with HITRAN and PNNL is very good (see Fig. 5). All structures of the PNNL spectrum are well reproduced for line positions and line intensities (bottom panels of Fig. 5 for a zoomed comparison). According to Table 3, our theoretically integrated intensity and absorbance deviate from HITRAN by 1% and from PNNL by 2% only.

### 4.3. Region (III): 1600–2750 cm$^{-1}$

This spectral range has been analyzed in Lafferty et al. (2011), Ben Hassen et al. (2012) but is not included in the current HITRAN database. The strongest absorption corresponds to the combination bands as $\nu_7+\nu_8$, $\nu_6+\nu_{10}$, $\nu_4+\nu_8$ or $\nu_3+\nu_{10}$. Figures 6 and 7 show comparisons between the theoretically simulated and observed PNNL spectra, which nearly perfectly match theory and experiment, as is also confirmed by the very good agreement in the integrated absorbance of about 2.5% that is within the error margin of the experimental determination (see Table 3 and Figs. 6 and 7). We note that the instrumental noise in the 2650–2750 cm−1 interval (Fig. 7) does not have a noticeable effect on the integrated absorbance comparison that is dominated by much stronger bands in the lower wavenumber range.

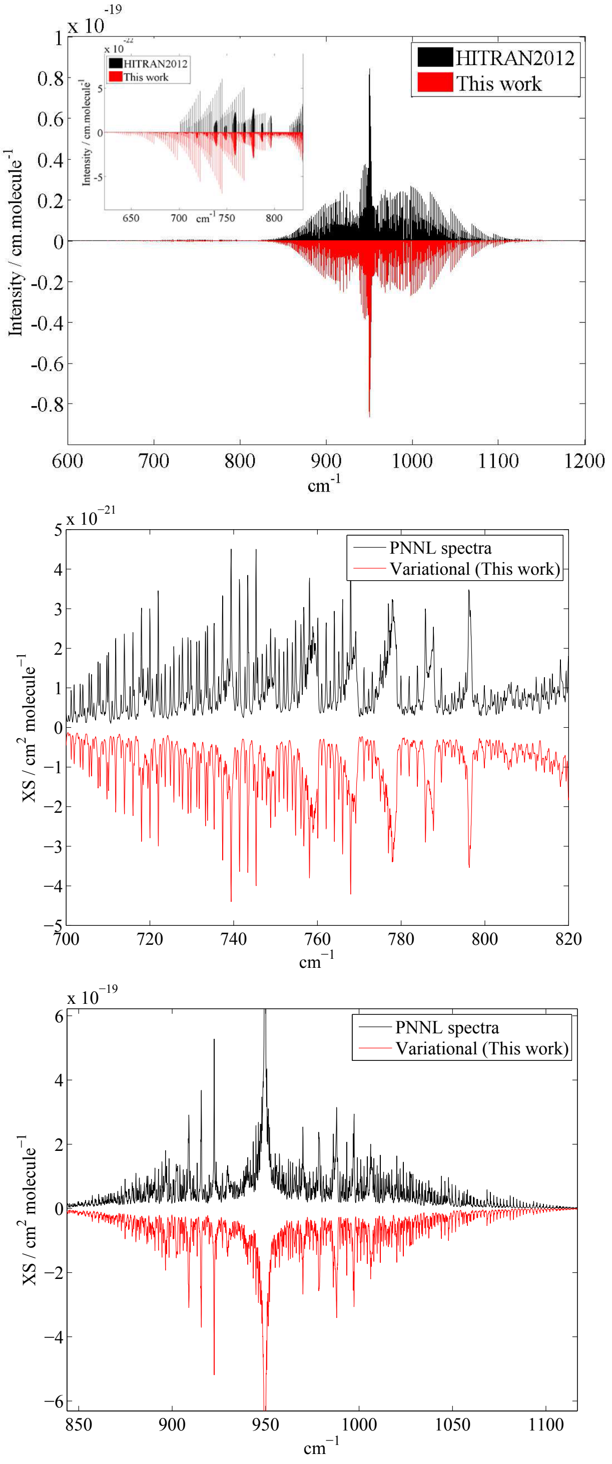

**Fig. 4.** Example comparison of theoretical absorption spectra of $^{12}C_2H_4$ with HITRAN and experimental PNNL records at room temperature in region I (see Fig. 3). Cross-sections (XS) are simulated with a resolution of 0.01 cm$^{-1}$ and a pressure of 1 atm. The PNNL absorbance was converted into cross sections (in cm$^2$/molecule) using the factor $9.28697 \times 10^{-16}$.

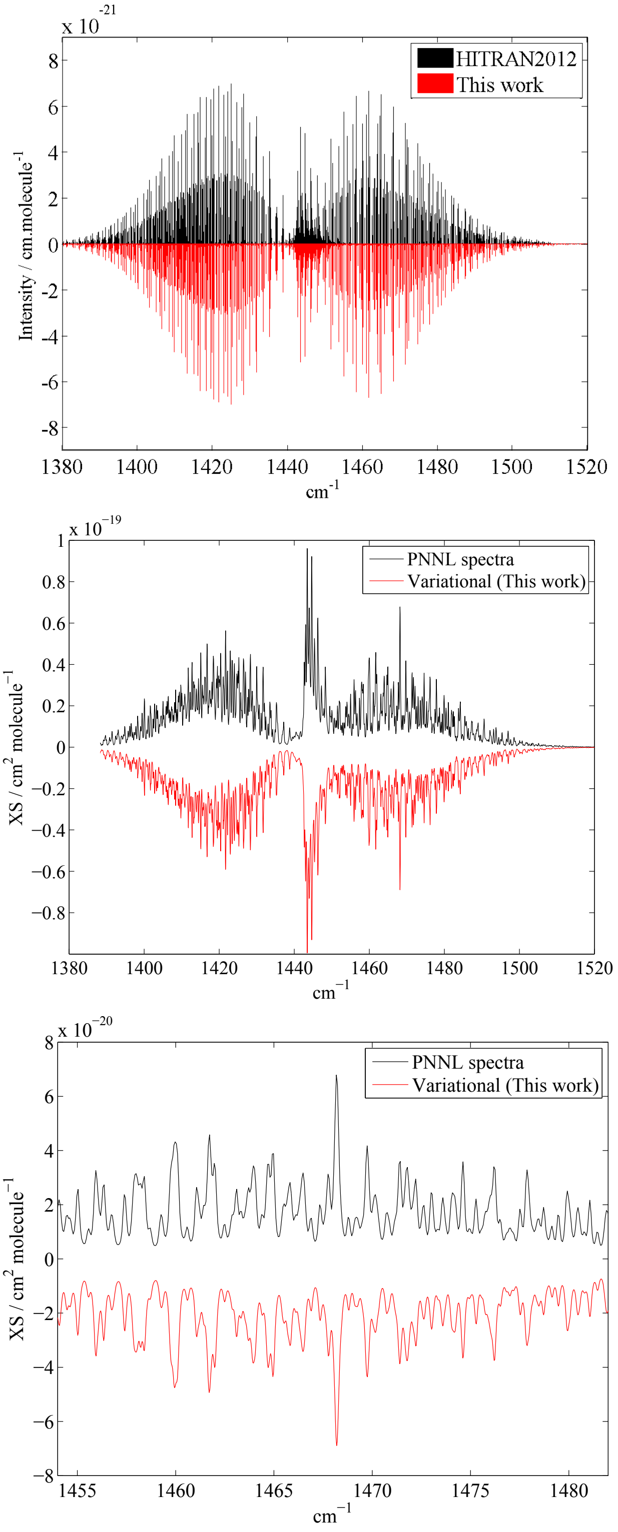

**Fig. 5.** Example comparison of theoretical absorption spectra of $^{12}C_2H_4$ with HITRAN and experimental PNNL records at room temperature in region II (see Fig. 3).

### 4.4. Region (IV): 2750–3450 cm$^{-1}$

The 3 $\mu$m region is probably one of the most important regions for probing atmospheres of various astrophysical objects. It is generally dominated by strong absorption bands of small hydrocarbons, corresponding to the vibrational frequencies of the C-H bonds. For ethylene, the two strongest bands associated with C-H stretching modes are $\nu_9$ and $\nu_{11}$. The HITRAN database lists about 6900 lines in this spectral range, 930 of which are assigned to the combination bands ($2\nu_{10}+\nu_{12}/\nu_2+\nu_{12}$), 140 to the hot band $\nu_9+\nu_{10}-\nu_{10}$ , and 4400 to the fundamental bands ($\nu_9/\nu_{11}$). The remaining lines (~1400) are not assigned in

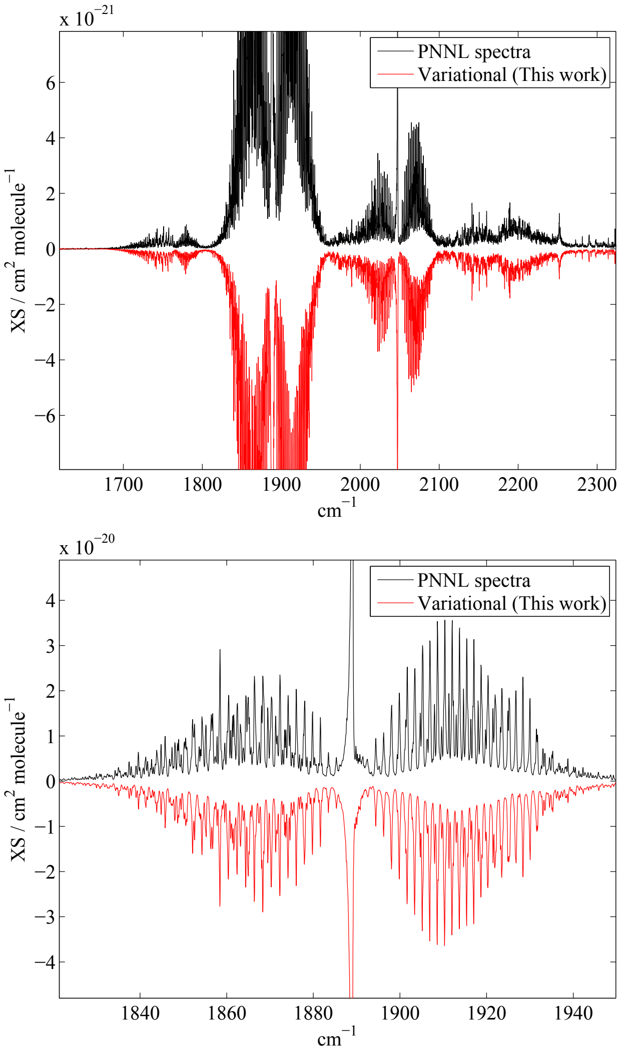

**Fig. 6.** Example comparison of theoretical absorption spectra of $^{12}C_2H_4$ with experimental PNNL records at room temperature in region III (see Fig. 3).

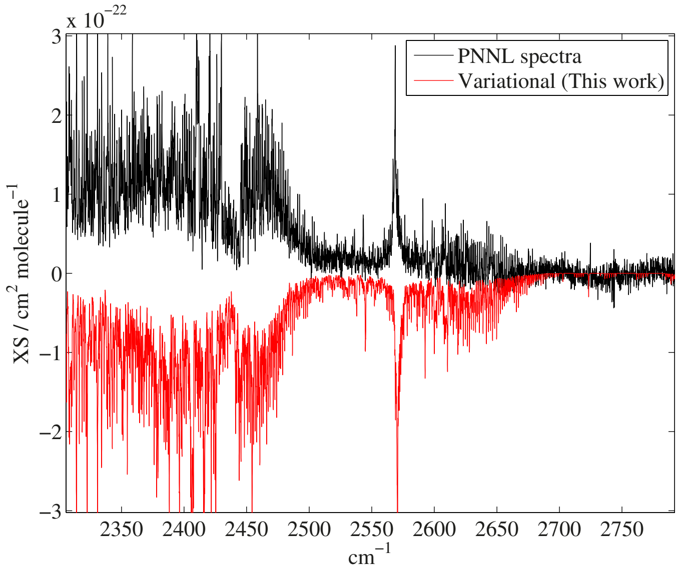

**Fig. 7.** Example comparison of theoretical absorption spectra of $^{12}C_2H_4$ with experimental PNNL records at room temperature in region III (see Fig. 3).

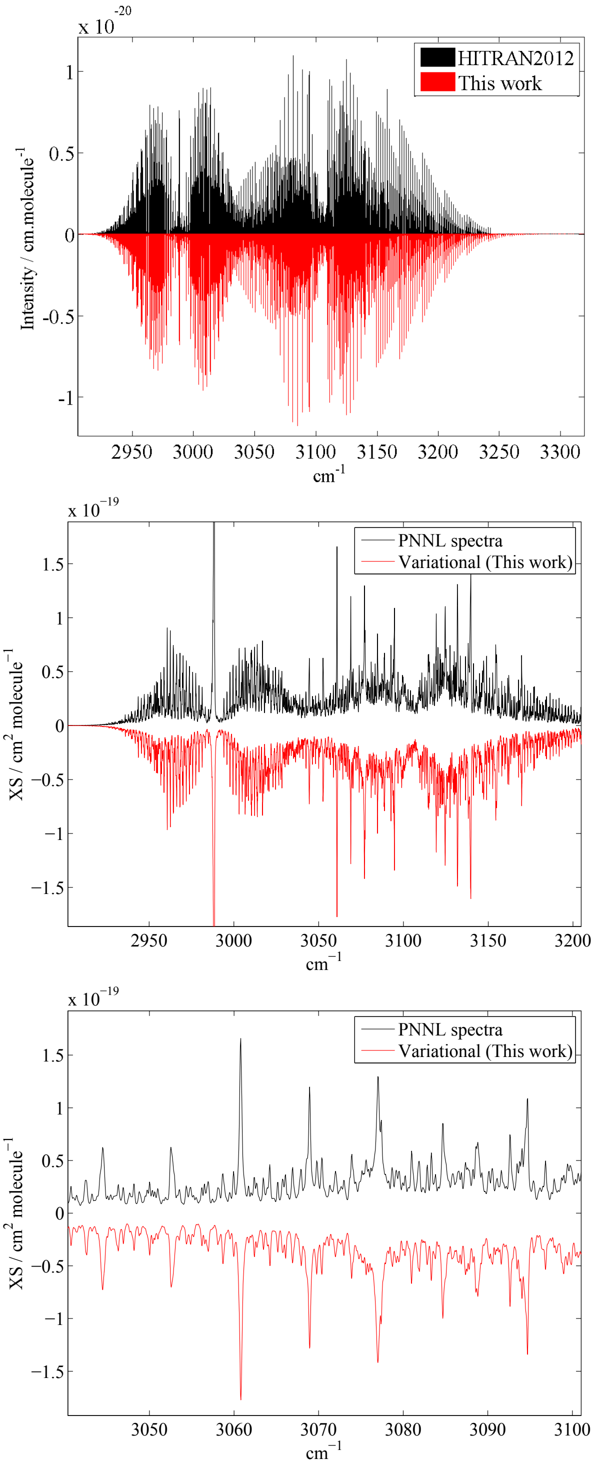

**Fig. 8.** Example comparison of theoretical absorption spectra of $^{12}C_2H_4$ with HITRAN and experimental PNNL records at room temperature in region IV (see Fig. 3).

HITRAN. In our predictions, about 1 100 000 lines are included at an intensity cutoff $10^{-26}$ cm/molecule with a CB/HB ratio of 1:10. Figure 8 displays an overall agreement with HITRAN and PNNL; the lower panels provide a zoomed scale comparison. A comparison with the integrated intensity (see Table 3) indicates that HITRAN underestimates our values by 18%, while our integrated absorbance agrees very well with PNNL (the deviation is lower than 1%). This means that an important part of the information on medium and weaker lines is lacking in HITRAN2012,

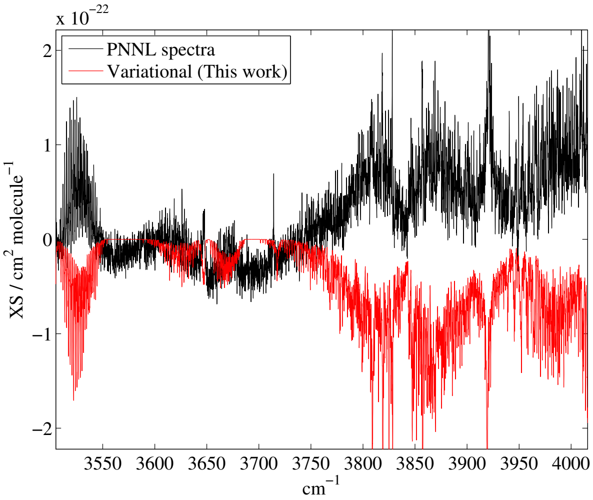

**Fig. 9.** Example comparison of theoretical absorption spectra of $^{12}C_2H_4$ with experimental PNNL records at room temperature in region V (see Fig. 3).

which is also proven by the comparison of the number of included transitions. Even when we apply the same intensity cutoff $I_{\max} = 10^{-24}$ cm/molecule as in HITRAN2012 in the range 2917–3242 $cm^{-1}$, we have a larger sample of 23848 transitions with an integrated range intensity of $6.61 \times 10^{-18}$ cm/molecule, which are to be compared to 6881 HITRAN transitions. This results in an integrated intensity of $5.78 \times 10^{-18}$ cm/molecule. The total number of lines also proves that information is lacking in HITRAN.

### *4.5. Region (V): 3450–4050 $cm^{-1}$*

This spectral range corresponds to the weakest absorption region in this study (Fig. 9). A detailed comparison with experimental PNNL spectra is quite delicate, however, because of low signal-to-noise ratio in experimental recordings the baseline in the PNNL spectra fluctuates quite strongly and becomes negative in some intervals, which might be attributed to some instrumental problems. However, the qualitative agreement remains acceptable. In Table 3 we omitted a comparison with unreliably measured integrated absorbance because of fringes, a quite high noise level, and instrumental effects in PNNL data between 3350 and 3800 $cm^{-1}$.

### *4.6. Region (VI): 4050–5200 $cm^{-1}$*

The $\nu_5 + \nu_{12}$ band near 2.2 $\mu$m have been analyzed in Ulenikov et al. (2010) for line positions. No intensity calculations have been reported in this region in the literature. Our calculations represent the first line-by-line intensity study in this spectral interval. Figure 10 shows that our predictions agree well with PNNL observations both overall and for more detailed comparisons.

### *4.7. Region (VI): 5200–6400 $cm^{-1}$*

This is the highest wavenumber range available in the PNNL room-*T* library. Although the 1.6 $\mu$m region is important for various applications, no line-by-line intensity information is compiled in the existing databases and in published analyses.

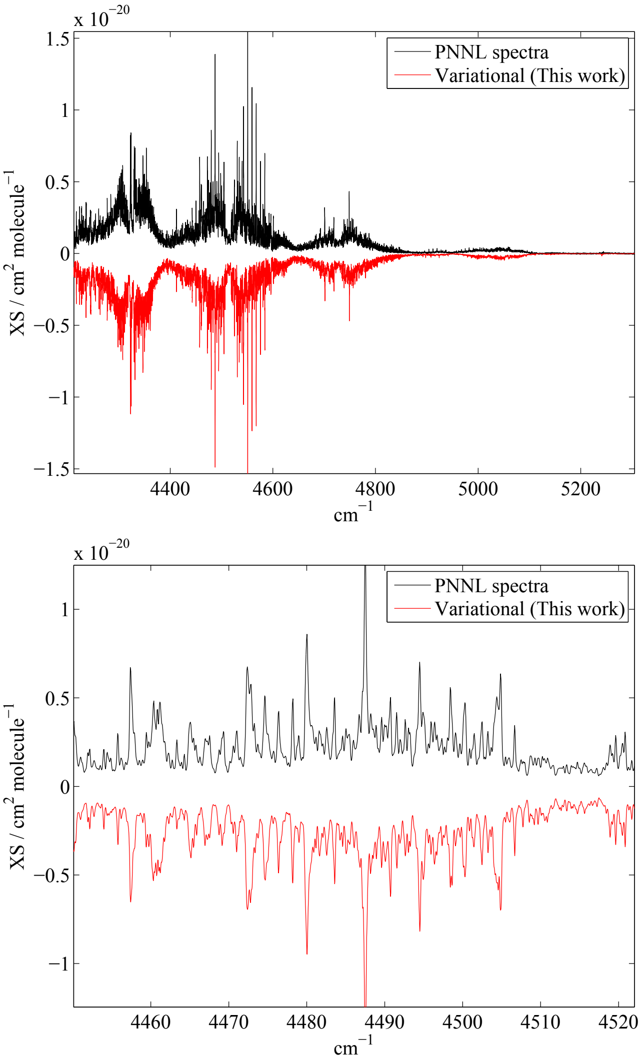

**Fig. 10.** Example comparison of theoretical absorption spectra of $^{12}C_2H_4$ with experimental PNNL records at room temperature in region VI (see Fig. 3).

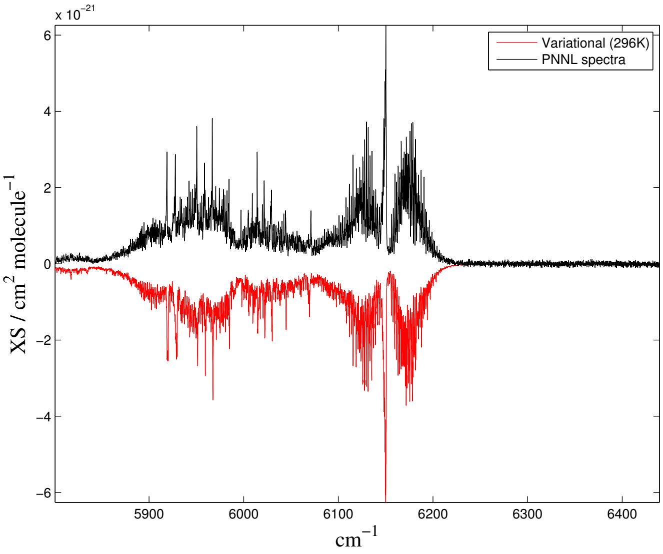

**Fig. 11.** Example comparison of theoretical absorption spectra of $^{12}C_2H_4$ with experimental PNNL records at room temperature in region VII (see Fig. 3).

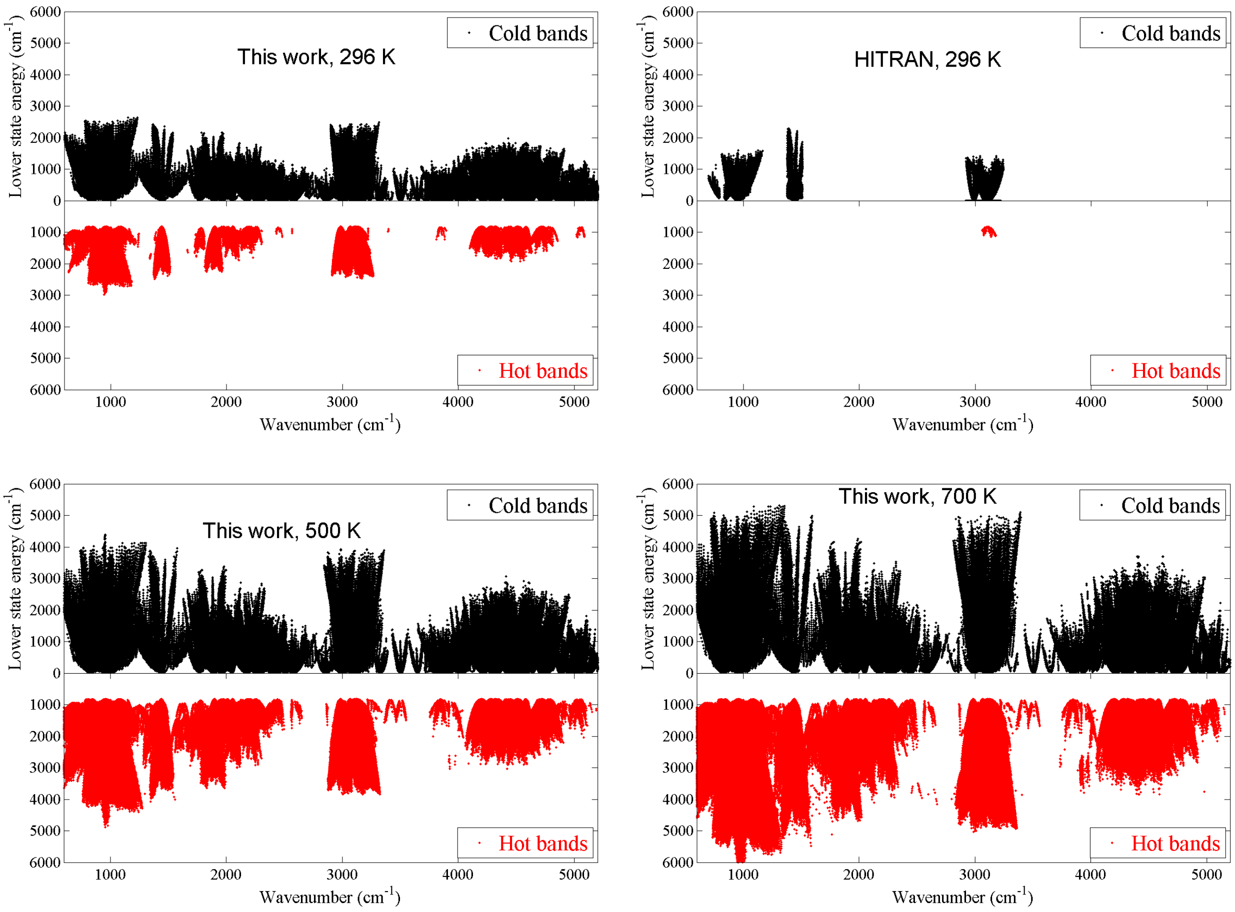

**Fig. 12.** Comparison of the lower energies involved in the database transitions between theoretical predictions (this work, at 296, 500, and 700 K) and HITRAN 2012 (296 K) and contribution of the cold and hot bands. The intensity cutoff was fixed to $5 \times 10^{-24}$ cm/mol to avoid overcrowded levels.

Figure 11 shows a qualitatively good agreement of our predictions with PNNL observations.

## 5. Temperature effects

### 5.1. Comparison of the lower level sets involved in line lists as a function of temperature

Extension to high-$T$ predictions is quite a challenge as higher polyads and $J$ states are populated. The two upper panels of Fig. 12 give an overview of lower energy levels involved in the transitions of our variational list and of HITRAN2012 with an intensity cutoff $I_{\rm min} = 5 \times 10^{-24}$ cm/molecule. The two lower panels illustrate a drastic increase in the lower levels, which is necessary to include in transitions at $T = 500$ K and $T = 700$ K with the same intensity cutoff. To have opacity calculations converged at these high temperatures, however, many more weaker transitions (up to ~60 millions lines) have to be considered down to $I_{\rm min} \sim 10^{-27}$ cm/molecule, as discussed in Sect. 6. A huge number of corresponding levels would not fit the scale of Fig. 12 that would be too crowded using this cutoff.

### 5.2. Spectra at cold-temperature conditions down to 80 K

At low temperatures, which are typically found in the atmospheres of the solar planets, the low-$J$ spectral transitions dominate, causing the bands to appear more compact, as illustrated in the three panels of Fig. 13 in the ranges 600–820 cm$^{-1}$, 800–1100 cm$^{-1}$ , and 1300–1500 cm$^{-1}$ for $T = 296$ K, 160 K, and 80 K. Similar changes in the ranges from 2300 cm$^{-1}$ to 3300 cm$^{-1}$ are shown in Fig. 14. To our knowledge, such low-temperature laboratory intensity or transmittance measurements, which could be used for a systematic validation of ab initio intensities in these conditions, do not exist. For methane, our low-$T$ line lists (Rey et al. 2016) computed with the same theoretical methods down to $T = 80$ K, have recently been used by Bézard (2016) to simulate the transmittance in the Titan atmosphere. This has yielded a good general agreement with observations explored by the Cassini-Huygens space mission with the Descent Imager/Spectral Radiometer (DISR) on the Huygens probe at various altitudes.

### 5.3. Spectra at high-temperature conditions up to 700 K

For elevated temperatures, the spectrum is dominated by higher-$J$ transitions and becomes much more congested with a rapidly increasing number of hot-band lines. The transparency windows between strong absorption intervals displayed in Fig. 3 become narrower or disappear almost entirely. The variation of the spectrum with temperatures in the far-infrared from 800 to 5000 cm$^{-1}$ is shown in Fig. 15 with examples of $T = 296$ K,

**Table 4.** Convergence of the integrated intensities Σ (× $10^{-17}$ cm/molecules) as a function of the cutoffs on the lower energy $E$ (in $\text{cm}^{-1}$), the line intensity $I$ (in cm/molecule), and the rotational quantum number $J$.

| | Wavenumbers ≤ 6400 $\text{cm}^{-1}$ | | | Wavenumbers ≤ 5200 $\text{cm}^{-1}$ | |
|---|---|---|---|---|---|
| $T$ | 80 K | 160 K | 296 K | 500 K | 700 K |
| Lower energy cut-off | Integrated intensities | | | | |
| $E \leq 500$ | 2.551 | 2.473 | 1.969 | 0.986 | 0.413 |
| $E \leq 1000$ | 2.553 | 2.549 | 2.382 | 1.516 | 0.752 |
| $E \leq 2000$ | 2.553 | 2.552 | 2.545 | 2.255 | 1.580 |
| $E \leq 3000$ | | 2.552 | 2.552 | 2.468 | 2.117 |
| $E \leq 4000$ | | | 2.552 | 2.512 | 2.381 |
| $E \leq 5000$ | | | | 2.517 | 2.475 |
| $E \leq 6000$ | | | | 2.518 | 2.494 |
| $E \leq 7000$ | | | | | 2.496 |
| Intensity cutoff | | | | | |
| $I \geq 10^{-21}$ | 2.281 | 2.152 | 1.853 | 1.052 | 0.363 |
| $I \geq 10^{-22}$ | 2.475 | 2.425 | 2.278 | 1.804 | 1.142 |
| $I \geq 10^{-23}$ | 2.533 | 2.517 | 2.463 | 2.231 | 1.799 |
| $I \geq 10^{-24}$ | 2.548 | 2.544 | 2.525 | 2.414 | 2.189 |
| $I \geq 10^{-25}$ | 2.552 | 2.550 | 2.545 | 2.489 | 2.387 |
| $I \geq 5 \times 10^{-26}$ | 2.553 | 2.551 | 2.548 | 2.501 | 2.423 |
| $I \geq 10^{-26}$ | | 2.552 | 2.552 | 2.518 | 2.479 |
| $I \geq 5 \times 10^{-27}$ | | | | | 2.496 |
| Rotational cutoff | | | | | |
| $J \leq 15$ | 2.499 | 2.167 | 1.591 | 1.051 | 0.762 |
| $J \leq 20$ | 2.550 | 2.464 | 2.120 | 1.622 | 1.258 |
| $J \leq 30$ | 2.553 | 2.551 | 2.506 | 2.279 | 2.027 |
| $J \leq 40$ | | 2.552 | 2.550 | 2.480 | 2.373 |
| $J \leq 50$ | | | 2.552 | 2.514 | 2.474 |
| $J \leq 60$ | | | | 2.518 | 2.493 |
| $J \leq 71$ | | | | | 2.496 |
| Number of lines | 388 954 | 828 897 | 2 904 094 | 12 742 100 | 58 848 859 |

500 K, and 700 K. The PNNL experimental FTS absorbance spectrum at $T = 296$ K is given at the bottom of each panel in black. To our knowledge, neither experimental nor theoretical high-temperature line intensities in ethylene spectra have been published up to now. For methane our high-$T$ line lists (Rey et al. 2014b) computed with the same theoretical methods have been used by Hargreaves et al. (2015), who have measured emission and absorption $CH_4$ laboratory spectra at $T = 1000$ K around 3 $\mu$m. They concluded that of all existing lists, the best match to their observations was given by our ab initio predictions.

### 5.4. Integrated intensities of cold and hot bands

Figure 16 shows the repartition of integrated intensities between cold and hot bands at temperatures 80 K, 160 K, 296 K, 500 K, and 700 K in various spectral ranges defined in Sect. 4. At $T = 500$ K the contribution of hot bands to the global opacity becomes very significant, and at $T = 700$ K the hot bands dominate the spectrum. The values of integrated intensities in each interval and the number of corresponding transitions are given in Table 4. In this table, the integrated intensities are considered as "converged" when we were able to converge at three digits up to room-$T$ and at two digits for high $T$ conditions.

## 6. Discussion: opacity convergence and the quasi-continuum issue

As we discussed above, the particular feature of high-$T$ spectra of polyatomic molecules are the very many contributing lines that rapidly increase with temperature. This is because the Boltzmann population involves very highly excited vibration-rotation states with a huge amount of allowed transitions. For example, our recent theoretical line list of methane $^{12}CH_4$ at $T = 2000$ K in the range 0–5000 $\text{cm}^{-1}$ included 11.5 billion transitions (Rey et al. 2014b), which were necessary to let the opacity calculation converge properly at this temperature. Most of these transitions correspond to hot bands of the excited vibrational states. As Hargreaves et al. (2012), Rey et al. (2014b) stated, the contributions of the tremendous number of weak transitions in methane spectra for $T > 1000$ K form a kind of quasi-continuum: the spectral density can reach $10^6$ lines per $\text{cm}^{-1}$ for the intensity cutoff $10^{-27}$ cm/molecule (see Fig. 3 of Rey et al. 2014b). An experimental measurement of individual line intensities of these overlapping transitions is clearly not feasible. The existing versions of spectral line lists such as HITRAN and GEISA, which are based on analyses of experimental laboratory spectra, do not include this information and cannot provide a correct modeling of radiative properties at high-temperature conditions as are typical for exoplanet atmospheres. As was argued in the recent review by Bernath (2014), which was devoted to

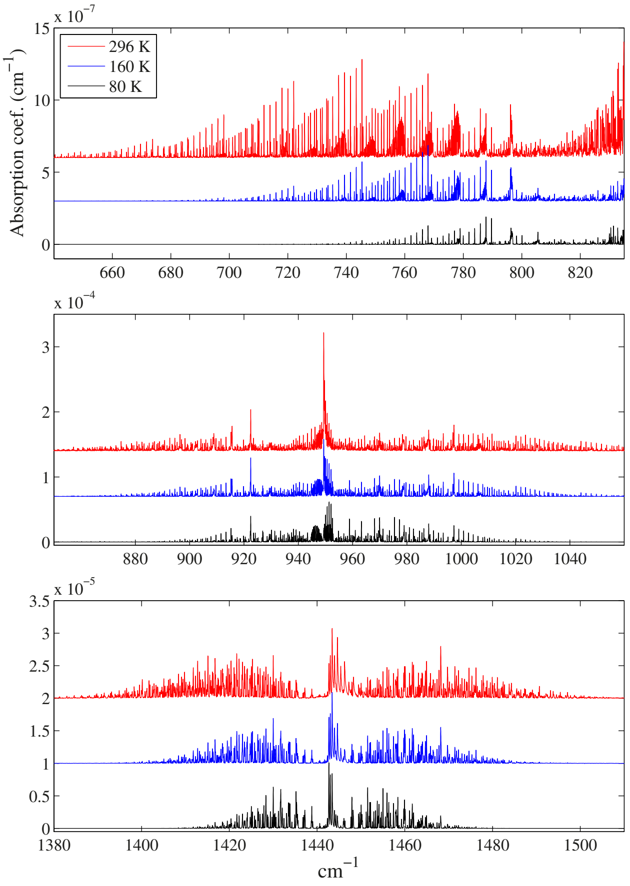

**Fig. 13.** Temperature effects (from 80 to 296 k) on the absorption coefficients in regions I and II. The spectra are computed with a Voigt line profile at a resolution of 0.01 cm$^{-1}$ and a pressure of 1 atm.

measurements of high-$T$ spectra, this information must be provided by theory.

At a given temperature, the number of transitions is larger for ethylene than for methane because of the three additional vibrational degrees of freedom and smaller rotational constants. Consequently the high-temperature ethylene spectra should be more congested. In Table 4 we give the results of the ethylene opacity convergence analysis for five temperatures between 80 K and 700 K as a function of three principal cutoff criteria: on the lowest individual line intensity ($I_{\min}$), on the energy of the lower state ($E_{\text{low}}$) for each transition, and on the maximum rotational quantum number $J$. We give here the line statistics up to 296 K in the full studied wavenumber range up to 6400 cm$^{-1}$ and up to 700 K in the range below 5200 cm$^{-1}$. This table is to be compared with the corresponding Table 4 of Rey et al. (2014b) for the methane molecule. At this stage, we were not able to go as far in temperature as for methane since ethylene calculations are much more demanding. For 700 K our calculations fully converge with respect to $E_{\text{low}}$ and to the rotational quantum number (up to $J_{\max} = 71$), whereas for methane $J_{\max} = 35$ was sufficient at the same temperature. Using the intensity cutoff of $I_{\min} = 5 \times 10^{-27}$ cm/molecule, the global opacity calculations converge to about 1%, resulting in over 63 million transitions below 5200 cm$^{-1}$. At the cutoff of $10^{-27}$ or $10^{-29}$ cm/molecule, the ethylene list would be much heavier than that for methane and unpractical for a direct use. In the supplementary material we provide a light version of the lists with a cutoff of $5 \times 10^{-26}$ cm/molecule that contains all essential features in the spectrum. The data are given in the form of an absorption list. This can be easily converted into emission lines through the well-known relation (Hargreaves et al. 2012)

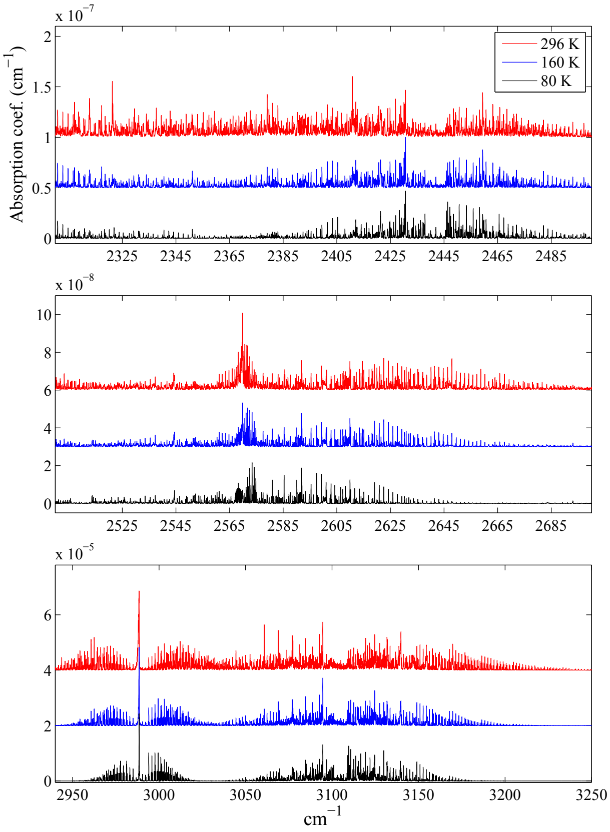

**Fig. 14.** Temperature effects (from 80 to 296 k) on the absorption coefficients in regions III and IV. The spectra are computed with a Voigt line profile at a resolution of 0.01 cm$^{-1}$ and a pressure of 1 atm.

$$S_e = S_a \nu^3 e^{-h\nu/kT}, \qquad (5)$$

where $S_a/S_e$ is the intensity of the absorbed or emitted line. The full version of the lists will be available through the TheoReTS information system (Rey et al. 2016)[2]. Comparison with experimental spectra carried out in this study has shown that the accuracy of band centers in our theoretical lists is better on average than 0.3 cm$^{-1}$ and the integrated absorbance errors are about 1–3%. Numerical tests suggest that our current ethylene data are sufficiently complete for use in the 50 K–700 K temperature range. The reported line lists could be also used at high-temperature conditions depending on the applications. When strong absorption or emission lines are required for remote-sensing ethylene detection, their intensities could be reliably converted into $T > 700$ K because the essential parts of HBs are included. This work can be qualitatively extrapolated to higher temperatures with some caution and by increasing the uncertainty margins. In contrast, for the radiative balance studies, the high $T$ extension requires caution because opacities might be lacking at transparency windows. In the latter case, this would require to include a higher energy cutoff. The above mentioned quasi-continuum ethylene absorption appear in many spectral intervals, starting with $T = 500$ K and higher. The TheoReTS information system provides a user-friendly graphical interface for a fast simulation of the absorption cross-sections

---

[2] Freely accessible at `http://theorets.univ-reims.fr` and `http://theorets.tsu.ru` web sites.

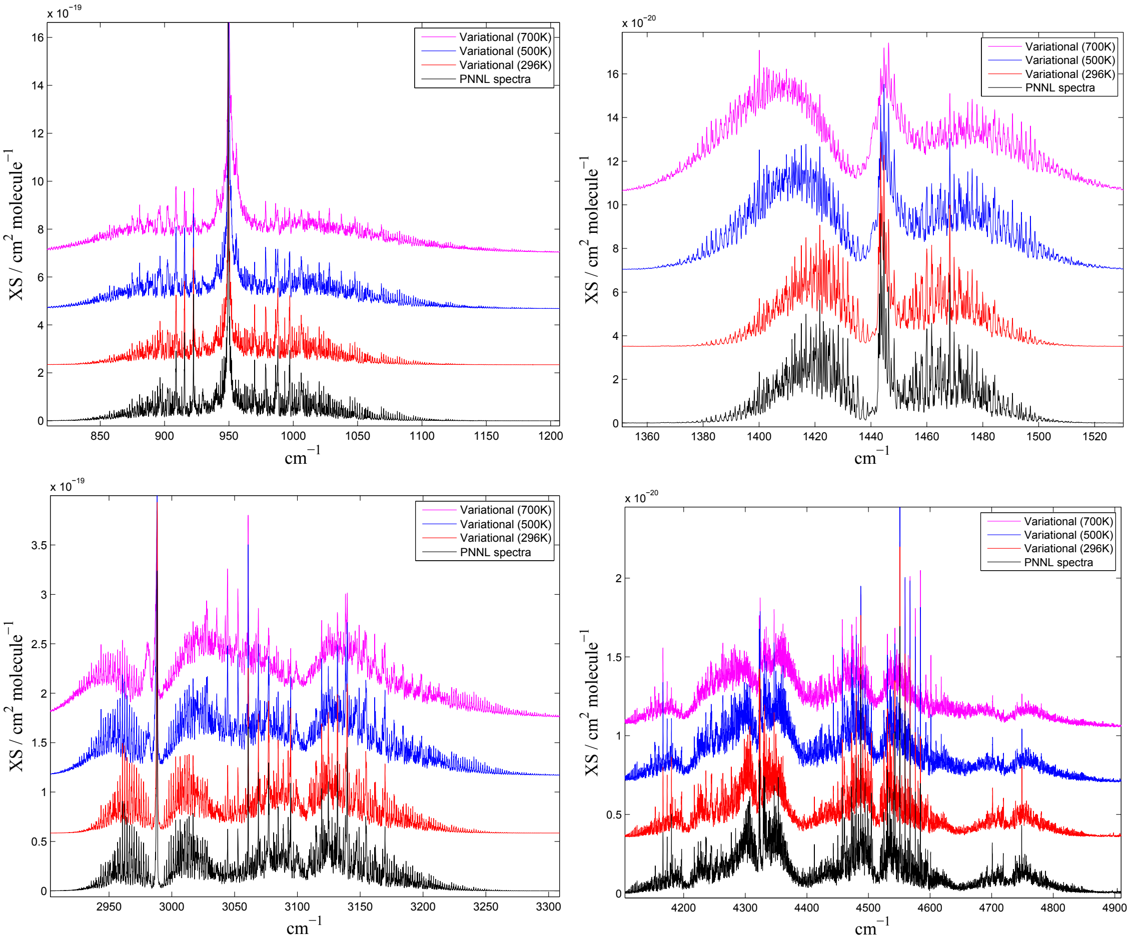

**Fig. 15.** Temperature effects (from 296 to 700 K) on the absorption XS in regions I and II, and IV and VI, and comparison with experimental PNNL records at room temperature. The spectra are computed with a Voigt line profile at a resolution of 0.01 $\mathrm{cm}^{-1}$ and a pressure of 1 atm. A self-broadening coefficient of 0.1 $\mathrm{cm}^{-1}\,\mathrm{atm}^{-1}$ was chosen.

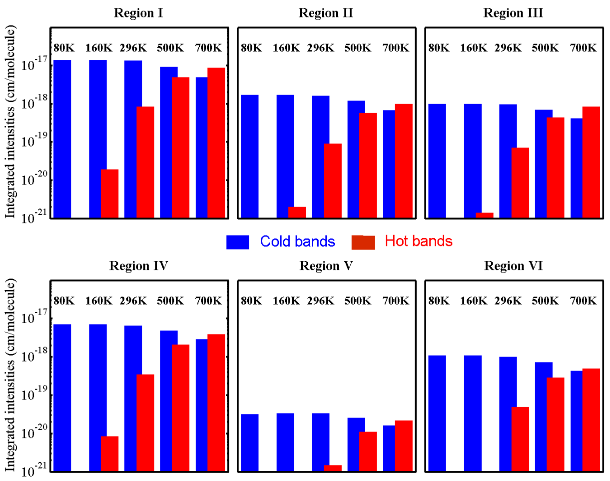

**Fig. 16.** Integrated intensities (in cm/molecule) for cold- and hot-band transitions from 80 to 700 K in regions I–VI.

and radiance accounting for the quasi-continuum using a computationally efficient super-lines approach as described in Rey et al. (2016). Further progress in the description of ethylene absorption or emission and for applications under various conditions would benefit from a broad collaboration of spectroscopists, theoretical chemists, specialists in the atmospheric modeling, and astrophysicists.

*Acknowledgements.* Support of the Tomsk State University Academic D. Mendeleev funding Program, of the French National Planetology program (PNP), of the LEFE Chat program of the "Institut National des Sciences de l'Univers" (CNRS) and of the Laboratoire International Franco-Russe "SAMIA" are acknowledged. A.V.N. acknowledges support of the Champagne-Ardenne region. We have benefited from the computational resources of the IDRIS/CINES computer centre of France, of the ROMEO computer centre Reims Champagne-Ardenne, and the computer centre SKIF Siberia (Tomsk).

## References

Abeles, F. B., Morgan, P. W., & Saltveit, M. E. J. 1992, Ethylene in Plant Biology (London: Academic Press)
Alkadrou, A., Bourgois, M. T., Rotger, M., Boudon, V., & Vander Auwera, J. 2016, J. Quant. Spectr. Rad. Transf., 182, 158
Avila, G., & Carrington Jr., T. 2011, J. Chem. Phys., 135, 064101
Ba, Y. A., Wenger, C., Surleau, R., et al. 2013, J. Quant. Spectr. Rad. Transf., 130, 62
Bach, M., Georges, R., Herman, M., & Perrin, A. 1999, Mol. Phys., 97, 265
Barber, R. J., Tennyson, J., Harris, G. J., & Tolchenov, R. N. 2011, MNRAS, 368, 1087
Ben Hassen, A., Kwabia Tchana, F., Flaud, J.-M., et al. 2012, J. Mol. Spectr., 282, 30
Bernath, P. F. 2014, Phil. Trans. R. Soc. A, 372, 20130087
Bézard, B., Moses, J. I., Lacy, J., et al. 2001, BAAS, 33, 1079
Blass, W., Hillman, J., Fayt, A., et al. 2001, J. Quant. Spectr. Rad. Transf., 71, 47
Bowman, J. M., Carter, S., & Handy, N. C. 2005, Progress in the quantum description of vibrational motion of polyatomic molecules (Elsevier B. V.)
Bunker, P. R., & Jensen, P. 1998, Molecular Symmetry and Spectroscopy (Ottawa: NRC-CNRC)
Canosa, A., Paramo, A., Le Picard, S., & Sims, I. 2007, Icarus, 187, 558

Carter, S., Sharma, A. R., Bowman, J. M., Rosmus, P., & Tarroni, R. 2009, J. Chem. Phys., 131, 224106

Carter, S., Bowman, J. M., & Handy, N. C. 2012a, Mol. Phys., 110, 775

Carter, S., Sharma, A., & Bowman, J. 2012b, J. Chem. Phys., 137

Cassam-Chenaï, P., Bouret, Y., Rey, M., et al. 2012, Int. J. Quantum Chem., 112, 2201

Cooper, G., Olney, T., & Brion, C. 1995, Chem. Phys., 194, 175

Cours, T., Rosmus, P., & Tyuterev, V. G. 2002, J. Chem. Phys., 117, 5192

Coustenis, A., & Bézard, B. 1995, Icarus, 115, 126

Coustenis, A., Bézard, B., & Gautier, D. 1989, Icarus, 80, 54

Coustenis, A., Bézard, B., Gautier, D., Marten, A., & Samuelson, R. 1991, Icarus, 89, 152

Coustenis, A., Achterberg, R., Conrath, B., et al. 2007, Icarus, 189, 35

Császár, A. G., Mátyus, E., Szidarovszky, T., et al. 2010, J. Quant. Spectr. Rad. Transf., 111, 1043

Dam, N., Engeln, R., Reuss, J., Pine, A., & Fayt, A. 1990, J. Mol. Spectr., 139, 215

Delahaye, T., Nikitin, A. V., Rey, M., Szalay, P. G., & Tyuterev, V. G. 2014, J. Chem. Phys., 141, 104301

Delahaye, T., Nikitin, A., Rey, M., Szalay, P., & Tyuterev, V. 2015, Chem. Phys. Lett., 639, 275

De Vleeschouwer, M., Lambeau, C., Fayt, A., & Meyer, C. 1982, J. Mol. Spectr., 93, 405

Dubernet-Tuckey, M., Antony, B., Ba, Y., et al. 2016, J. Phys. B, in press

Flaud, J.-M., Lafferty, W., Sams, R., & Malathy Devi, V. 2010, J. Mol. Spectr., 259, 39

Flaud, J.-M., Lafferty, W., Malathy Devi, V., Sams, R., & Chris Benner, D. 2011, J. Mol. Spectr., 267, 3

Gabona, M., & Tan, T. 2014a, J. Mol. Spectr., 299, 35

Gabona, M., & Tan, T. 2014b, J. Mol. Spectr., 299, 31

Gabona, M., Tan, T., & Woo, J. 2014, J. Mol. Spectr., 305, 22

Georges, R., Bach, M., & Herman, M. 1999, Mol. Phys., 97, 279

Goode, J. G., Yokelson, R. J., Susott, R. A., & Ward, D. E. 1999, J. Geophys. Res. Atmos., 104, 21237

Griffith, C., Bézard, B., Greathouse, T., et al. 1997, Icarus, 128, 275

Hargreaves, R. J., Beale, C. A., Michaux, L., Irfan, M., & Bernath, P. F. 2012, ApJ, 757, 46

Hargreaves, R., Bernath, P., Bailey, J., & Dulick, M. 2015, ApJ, 813

Hesman, B., Bjoraker, G., Sada, P., et al. 2012, ApJ, 760

Holland, D., Shaw, D., Hayes, M., et al. 1997, Chem. Phys., 219, 91

Hu, R., & Seager, S. 2014, ApJ, 784

Huang, X., Schwenke, D. W., & Lee, T. J. 2011a, J. Chem. Phys., 134, 044320

Huang, X., Schwenke, D. W., & Lee, T. J. 2011b, J. Chem. Phys., 134, 044321

Huang, X., Schwenke, D. W., Tashkun, S. A., & Lee, T. J. 2012, J. Chem. Phys., 136, 124311

Huang, X., Freedman, R. S., Tashkun, S. A., Schwenke, D. W., & Lee, T. J. 2013, J. Quant. Spectr. Rad. Transf., 130, 134

Huang, X., Gamache, R. R., Freedman, R. S., Schwenke, D. W., & Lee, T. J. 2014, J. Quant. Spectr. Rad. Transf., 147, 134

Jacquinet-Husson, N., Crepeau, L., Armante, R., et al. 2011, J. Quant. Spectr. Rad. Transf., 112, 2395

Johnson, T., Sams, R., & Sharpe, S. 2004, Proc. SPIE – The Int. Soc. Opt. Eng., 5269, 159

Kostiuk, T., Espenak, F., Mumma, M., & Romani, P. 1989, Infrared Phys., 29, 199

Lafferty, W., Flaud, J.-M., & Tchana, F. 2011, Mol. Phys., 109, 2501

Lambeau, C., De Vleeschouwer, M., Van Lerberghe, D., et al. 1982, Mol. Phys., 46, 981

Lebron, G. B., & Tan, T. L. 2012, Int. J. Spectr., 2012, 1

Li, J., Carter, S., Bowman, J. M., et al. 2014, J. Phys. Chem. Lett., 5, 2364

Lodi, L., Tennyson, J., & Polyansky, O. L. 2011, J. Chem. Phys., 135, 034113

Lorono, M., Boudon, V., Loete, M., et al. 2010, J. Quant. Spectr. Rad. Transf., 111, 2265

Maltagliati, L., Bézard, B., Vinatier, S., et al. 2015, Icarus, 248, 1

Martin, J., Lee, T., Taylor, P., & Francois, J.-P. 1995, J. Chem. Phys., 103, 2589

Moses, J., Bézard, B., Lellouch, E., et al. 2000, Icarus, 143, 244

Nikitin, A. V., Holka, F., Tyuterev, V. G., & Fremont, J. 2009, J. Chem. Phys., 130, 244312

Nikitin, A. V., Rey, M., Champion, J. P., & Tyuterev, V. 2012, J. Quant. Spectr. Rad. Transf., 113, 1034

Nikitin, A. V., Rey, M., & Tyuterev, V. G. 2014, J. Mol. Spectr., 305, 40

Nixon, C., Achterberg, R., Conrath, B., et al. 2007, Icarus, 188, 47

Oomens, J., Oudejans, L., Reuss, J., & Fayt, A. 1994a, Eur. Quantum Electronics Conf., Technical Digest, 284

Oomens, J., Oudejans, L., Reuss, J., & Fayt, A. 1994b, Chem. Phys., 187, 57

Oomens, J., Reuss, J., Mellau, G., et al. 1996, J. Mol. Spectr., 180, 236

Partridge, H., & Schwenke, D. W. 1997, J. Chem. Phys., 106, 4618

Perevalov, V. I., Tyuterev, V., & Zhilinskii, B. I. 1984, Chem. Phys. Lett., 104, 455

Perevalov, V. I., Tyuterev, V., & Zhilinskii, B. I. 1985, J. Mol. Spectr., 111, 1

Rey, M., Nikitin, A. V., & Tyuterev, V. G. 2010, Mol. Phys., 108, 2121

Rey, M., Nikitin, A. V., & Tyuterev, V. G. 2012, J. Chem. Phys., 136, 244106

Rey, M., Nikitin, A. V., & Tyuterev, V. G. 2013a, Phys. Chem. Chem. Phys., 15, 10049

Rey, M., Nikitin, A. V., & Tyuterev, V. G. 2013b, J. Mol. Spectr., 291, 85

Rey, M., Nikitin, A. V., & Tyuterev, V. G. 2014a, J. Chem. Phys., 141, 044316

Rey, M., Nikitin, A. V., & Tyuterev, V. G. 2014b, ApJ, 789, 2

Rey, M., Nikitin, A. V., & Tyuterev, V. G. 2015a, J. Phys. Chem. A, 119, 4763

Rey, M., Nikitin, A. V., & Tyuterev, V. G. 2015b, J. Quant. Spectr. Rad. Transf., 164, 207

Rey, M., Nikitin, A., Babikov, Y., & Tyuterev, V. 2016, J. Mol. Spectr., in press

Rinsland, C. P., Paton-Walsh, C., Jones, N. B., et al. 2009, J. Quant. Spectr. Rad. Transf., 96, 301

Rixon, G., Dubernet, M., Piskunov, N., et al. 2011, AIP Conf. Proc., 1344, 107

Roe, H., de Pater, I., & McKay, C. 2004, Icarus, 169, 440

Romani, P., Jennings, D., Bjoraker, G., et al. 2008, Icarus, 198, 420

Rotger, M., Boudon, V., & Vander Auwera, J. 2008, J. Quant. Spectr. Rad. Transf., 109, 952

Rothman, L. S., Gordon, I. E., Babikov, Y., et al. 2013, J. Quant. Spectr. Rad. Transf., 130, 4

Rusinek, E., Fichoux, H., Khelkhal, M., et al. 1998, J. Mol. Spectr., 189, 64

Sada, P., Bjoraker, G., Jennings, D., McCabe, G., & Romani, P. 1998, Icarus, 136, 192

Sada, P., Bjoraker, G., Jennings, D., Romani, P., & McCabe, G. 2005, Icarus, 173, 499

Sartakov, B., Oomens, J., Reuss, J., & Fayt, A. 1997, J. Mol. Spectr., 185, 31

Schulz, B., Encrenaz, T., Bézard, B., et al. 1999, A&A, 350, 13

Schwenke, D. W. 2002, Spectrochim. Acta – Part Mol. Biomol. Spectr., 58, 849

Schwenke, D. W., & Partridge, H. 2001, Spectrochim. Acta – Part Mol. Biomol. Spectr., 57, 887

Sousa-Silva, C., Hesketh, N., Yurchenko, S. N., Hill, C., & Tennyson, J. 2014, J. Quant. Spectr. Rad. Transf., 142, 66

Swain, M. R., Deroo, P., Griffith, C. A., et al. 2010, Nature, 463, 637

Szalay, P. G., Holka, F., Fremont, J., et al. 2011, Phys. Chem. Chem. Phys., 13, 3654

Tan, T., & Gabona, M. 2012, J. Mol. Spectr., 275, 5

Tan, T., Lau, S., Ong, P., Goh, K., & Teo, H. 2000, J. Mol. Spectr., 203, 310

Tan, T., Gabona, M., Godfrey, P., & McNaughton, D. 2015a, J. Mol. Spectr., 307, 40

Tan, T., Ng, L., & Gabona, M. 2015b, J. Mol. Spectr., 312, 6

Tennyson, J., Hill, C., & Yurchenko, S. N. 2013, AIP Conf. Proc., 1545, 186

Tinetti, G., Encrenaz, T., & Coustenis, A. 2013, A&ARv, 21, 63

Tyuterev, V., Tashkun, S., Rey, M., et al. 2013a, J. Phys. Chem. A, 117, 13779

Tyuterev, V. G., Kochanov, R. V., Tashkun, S. A., Holka, F., & Szalay, P. G. 2013b, J. Chem. Phys., 139, 134307

Tyuterev, V., Kochanov, R., Campargue, A., et al. 2014, Phys. Rev. Lett., 113, 143002

Ulenikov, O. N., Onopenko, G. A., Bekhtereva, E. S., et al. 2010, Mol. Phys., 108, 637

Ulenikov, O., Gromova, O., Aslapovskaya, Y., & Horneman, V.-M. 2013, J. Quant. Spectr. Rad. Transf., 118, 14

Ulenikov, O., Gromova, O., Bekhtereva, E., et al. 2015, J. Quant. Spectr. Rad. Transf., 151, 224

Vander Auwera, J., Fayt, A., Tudorie, M., et al. 2014, J. Quant. Spectr. Rad. Transf., 148, 177

Vinatier, S., Bézard, B., Fouchet, T., et al. 2007, Icarus, 188, 120

Vinatier, S., Bézard, B., Nixon, C., et al. 2010, Icarus, 205, 559

Wang, C., Zielke, P., Sigurbjornsson, O., Viteri, C., & Signorell, R. 2009, J. Phys. Chem. A, 113, 11129

Wang, X. G., & Carrington Jr., T. 2013a, Mol. Phys., 111, 2320

Wang, X. G., & Carrington Jr., T. 2013b, J. Chem. Phys., 138, 104106

Warmbier, R., Schneider, R., Sharma, A. R., et al. 2009, A&A, 495, 655

Watson, J. K. G. 1968, Mol. Phys., 15, 479

Wu, C., Chen, F., & Judge, D. 2004, J. Geophys. Research E: Planets, 109, E07S15 1

Yang, Y., Li, Z., Zhao, Y., et al. 2012, Comp. Theor. Chem., 991, 66

Yurchenko, S. N., & Tennyson, J. 2014, MNRAS, 440, 1649

Yurchenko, S. N., Carvajal, M., Thiel, W., & Jensen, P. 2006, J. Mol. Spectr., 239, 71

Yurchenko, S. N., Thiel, W., & Jensen, P. 2007, J. Mol. Spectr., 245, 126

Yurchenko, S. N., Barber, R. J., Yachmenev, A., et al. 2009, J. Phys. Chem. A, 113, 11845

## Appendix: Technical aspects

*Refining the molecular force constants*: the force constant matrix $F$, together with the geometry-based Wilson matrix $G$, are used to determine the vibrational frequencies and the associated modes. The quantum-mechanical ab inito force constant matrix $F$ can typically be simply computed, but generally the eigenvalues of the $GF$ matrix may differ from the experimental measurements by some wavenumbers, typically 1−10 $\text{cm}^{-1}$ , depending on the electronic structure calculation method. If $\Lambda$ consists of a set of refined frequencies, we have to solve the inverse harmonic eigenvalue problem $GFL = L\Lambda$ to extract the $F$ matrix. This technical aspect is beyond the scope of the present paper and will be explained elsewhere. We provide here the new force constant matrices used for this work. They are given for each symmetry block as (in a.u. units)

$$F^{(A_g)} = \left(\begin{array}{r} 1.5611030.045557{-}0.068732 \\ 2.6099370.2731294 \\ 1.471659 \end{array}\right)$$

$$F^{(B_{2g})} = \left(\begin{array}{r} 1.5415690.106736 \\ 0.639798 \end{array}\right),\ F^{(B_{2u})} = 0.201629$$

$$F^{(B_{3u})} = \left(\begin{array}{r} 1.5517060.038784 \\ 0.457680 \end{array}\right),\ F^{(B_{3g})} = 0.146709$$

$$F^{(B_{1u})} = \left(\begin{array}{r} 1.559720{-}0.096896 \\ 1.361242 \end{array}\right),\ F^{(A_u)} = 0.279207.$$

All other high-order parameters of the PES were held fixed to their ab initio values.

*Hamiltonian model and basis set*: in contrast to commonly used empirical spectroscopic models that deal with finite-dimensional matrices, the variational calculations face the well-known problem of the basis-set convergence when increasing the number of atoms $N$, the vibrational excitation, and the value of the total angular momentum $J$. To overcome this limitation, a series of reduction and compression techniques were applied to the Hamiltonian and basis functions to enable calculations even for high $J$ values. In this work, the Hamiltonian model is that of Delahaye et al. (2014), while the vibrational and ro-vibrational basis sets were slightly improved to allow a better convergence. For the full vibrational problem, a modified $F(11)$ basis against $F(9)$ in Delahaye et al. (2014) was used (see Rey et al. (2015b) for a definition of the basis sets), the largest symmetry block to be diagonalized being of size 81800. The diagonalization of matrices for high $J$ values is very demanding in terms of memory and CPU time. To reduce the cost of this, a set of so-called reduced vibrational $F(5)$ and $F(6)$ basis were introduced, with largest sizes $N_v$ of 400 and 900, respectively. The size of the ro-vibrational matrices will thus grow roughly as $N_v \times (2J + 1)$.